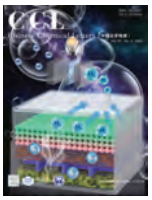
Chinese Chemical Letters 37 (2026) 111850

Contents lists available at ScienceDirect

Chinese Chemical Letters

journal homepage: www.elsevier.com/locate/cclet



Lignin valorization towards porous carbon cathodes in zinc ion hybrid capacitors

Caiwei Wang[a,b,*], Cheng Zeng[a], Changhong Wei[a], Guizhen Chen[a], Yueling Liang[a], Wenli Zhang[c,d,*]

[a] Guangxi Key Laboratory of Petrochemical Resource Processing and Process Intensification Technology, School of Chemistry and Chemical Engineering, Guangxi University (GXU), Nanning 530004, China
[b] University Engineering Research Center of Green Chemical New Materials, Nanning 530004, China
[c] School of Chemical Engineering and Light Industry, Guangdong Provincial Key Laboratory of Plant Resources Biorefinery, Guangdong University of Technology (GDUT), Guangzhou 510006, China
[d] Guangdong Provincial Laboratory of Chemistry and Fine Chemical Engineering Jieyang Center, Jieyang 515200, China

ARTICLE INFO

Article history:
Received 23 July 2025
Revised 9 September 2025
Accepted 17 September 2025
Available online 17 September 2025

Keywords:
Lignin
Porous carbons
Preparation methodology
Pore regulation
Surface modification
Morphology design
Zinc ion hybrid capacitors

ABSTRACT

Zinc ion hybrid capacitors (ZIHCs) are emerging electrochemical energy storage devices with the dual characteristics of high energy density and high power density. However, the mismatch of capacity and electrode kinetics between porous carbon cathodes and zinc metal anodes limits the development of ZIHCs. Lignin has high carbon content, high aromaticity, and three-dimensional functional molecular structures, which is an ideal raw material for preparing high-performance porous carbon electrode materials with high carbon yield, conductive carbon network and enriched heteroatom dopants. Currently, the high-value utilization ratio of industrial lignin is lower than 10%. In this review, the typical preparation methodologies of lignin-derived porous carbons are summarized. The latest research advances for the lignin-derived porous carbon cathodes in ZIHCs are critically focused from the perspectives of pore regulation, surface modification, and morphology design. The core points and development directions that lignin-derived porous carbon cathodes are expected to achieve an original breakthrough in the future are proposed from three levels of techniques, mechanisms, and applications. This review fills the blank region in the applications of lignin-derived porous carbons for ZIHCs, aiming to provide valuable guidance for the high-value utilization process of lignin and the industrialization process of ZIHCs.

© 2026 Published by Elsevier B.V. on behalf of Chinese Chemical Society and Institute of Materia Medica, Chinese Academy of Medical Sciences.

1. Introduction

Zinc ion hybrid capacitors (ZIHCs), composed of cheap zinc metal as anodes, low-cost porous carbon as cathodes, and high-safety aqueous electrolytes, are novel electrochemical energy storage devices [1–6]. Due to the hybrid characteristics of high-energy batteries and high-power supercapacitors [7–10], ZIHCs are becoming one of the most promising electrochemical energy storage technologies in the post-lithium battery era. As illustrated in Fig. 1, the development of ZIHCs is being unfortunately hindered by the capacity mismatch between porous carbon cathodes (100–350 mAh/g) and zinc (Zn) metal anodes (820 mAh/g) [11–14] and the kinetic mismatch between the slow electrode kinetics of Zn anodes and porous carbon cathodes [15].

Many review articles are dedicated to exploring solutions toward two key challenges on the development path of ZIHCs from the perspective of porous carbon cathodes [1,4,11,16–19]. However, due to the continuous research advancements in pore regulation [20–25], the key progress of porous carbon cathodes in ZIHCs needs to be supplemented. Furthermore, the difference in the overall microstructures of porous carbons from different types of carbon sources is significant, which may result in overly one-sided structure-performance relationships. If porous carbons are prepared from a single carbon source, the microstructural difference would be relatively reduced. Therefore, a precise and systematic structure-performance relationship will be obtained naturally.

As illustrated in Fig. 2, lignin is one of the important components in renewable biomass, acting as the role of binder. Compared with common carbon sources for the preparation of porous carbon cathodes, lignin has a high carbon content of up to 65%, which could achieve a high carbon yield. Furthermore, lignin has the unique specialty of high aromaticity [26–28], and

* Corresponding authors.
E-mail addresses: cwwang@gxu.edu.cn (C. Wang), wlzhang@gdut.edu.cn (W. Zhang).

https://doi.org/10.1016/j.cclet.2025.111850
1001-8417/© 2026 Published by Elsevier B.V. on behalf of Chinese Chemical Society and Institute of Materia Medica, Chinese Academy of Medical Sciences.

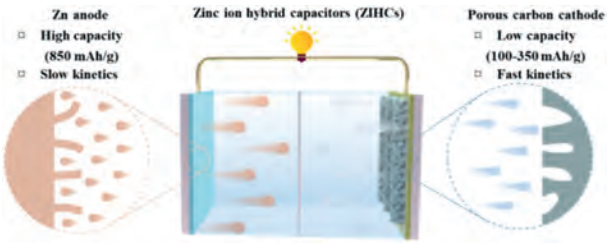


Fig. 1. Bottleneck problems for the development of ZIHCs.

three-dimensional functional molecular structures originating from oxidation [29,30], sulfonation [31,32] and amination [33] modifications, facilitating the formation of a highly conductive carbon network and the doping of functional heteroatoms. More importantly, industrial lignin mainly includes alkali lignin from the pulp industry and enzymatic hydrolysis lignin from the bioethanol industry [34]. The global annual yield of industrial lignin exceeds 50 million tons [35]. Most of the industrial lignin is used for combustion to provide heat and recover alkali reagents [36]. The high-value utilization ratio of industrial lignin is less than 10% [36,37]. Therefore, lignin is an ideal carbon source for preparing high-performance porous carbons, which is promising to break through the two bottlenecks for the development of ZIHCs. So far, there has been no review about the applications of lignin-derived porous carbons in ZIHCs.

This review first introduces typical preparation methodologies of lignin-derived porous carbons in brief. The latest research progress of lignin-derived porous carbon cathodes in ZIHCs are then summarized from the perspectives of pore regulation, surface modification, and morphology design. The future development directions of lignin-derived porous carbon cathodes are lastly proposed from three levels of techniques, mechanisms, and applications. The objective of this review is to promote the high-value utilization process of lignin resources and the industrialization process of ZIHCs.

2. Preparation methodologies of lignin-derived porous carbons

The carbonization process of lignin is mainly divided into three stages, *i.e.*, dehydration, pyrolysis, and graphitization. The dehydration stage occurs below 200 °C, where free water, adsorbed water, and bound water sequentially evolve with increasing temperature. The pyrolysis stage occurs between 200 °C and 500 °C, where the unstable β-O-4 bonds are first cleaved, followed by C-O and C-C bonds [38–42]. Functional groups such as methoxy, carboxyl, hydroxyl, amino, and sulfonic acid groups severely drop off, generating gases including CO_2, CO, CH_4, NH_3, SO_2 [43–48], which results in pore formation. Simultaneously, the aromatic rings freely polymerize to form graphene nanosheets [49], which randomly stack to form porous carbon skeletons. The elimination rate of heteroatoms becomes slow above 500 °C. With the increase in the carbonization temperature, the graphene sheets orderly rearrange into graphene nanocrystals, followed by evolving into long-range warped graphene microcrystals [50]. However, the proportion of sp^3 hybrid carbon in the highly heterogeneous aromatic structure of lignin is high [51], making it difficult to be eliminated during the carbonization process. This leads to high cross-linking of graphene microcrystals, hindering their large-scale ordered rearrangement, which makes it difficult to be highly graphitized even at high temperatures (>1000 °C) [52].

As illustrated in Table 1, the specific surface areas and total pore volumes of lignin-derived porous carbons prepared by direct carbonization first increase and then decrease, reaching the highest values at 800 °C and decreasing to below 5 m^2/g and 0.05 cm^3/g above 1200 °C, respectively [53]. The low porosity is attributed to the formation of graphene nanocrystals and tight stacking, followed by developing into long-range warped graphene microcrystals and closed nanopores [54,55].

The alkali lignin-derived porous carbons prepared by the direct carbonization at 800 °C show lower specific surface areas and total pore volumes than the enzymatic hydrolysis lignin-derived porous carbons [56]. Due to the spatial occupation effect of sulfates [57], the porous carbons prepared from sodium lignosulfonate and calcium lignosulfonate show slightly higher specific surface areas and total pore volumes than those prepared from enzymatic hydrolysis lignin and alkali lignin [58,59].

The lignin-derived porous carbons prepared by direct carbonization possess low specific surface area and total pore volume, exhibiting poor capacitive performance generally. Therefore, it is necessary to enrich the porosities of lignin-derived porous carbons. The preparation methodologies of lignin-derived porous carbons mainly include chemical activation and template methods.

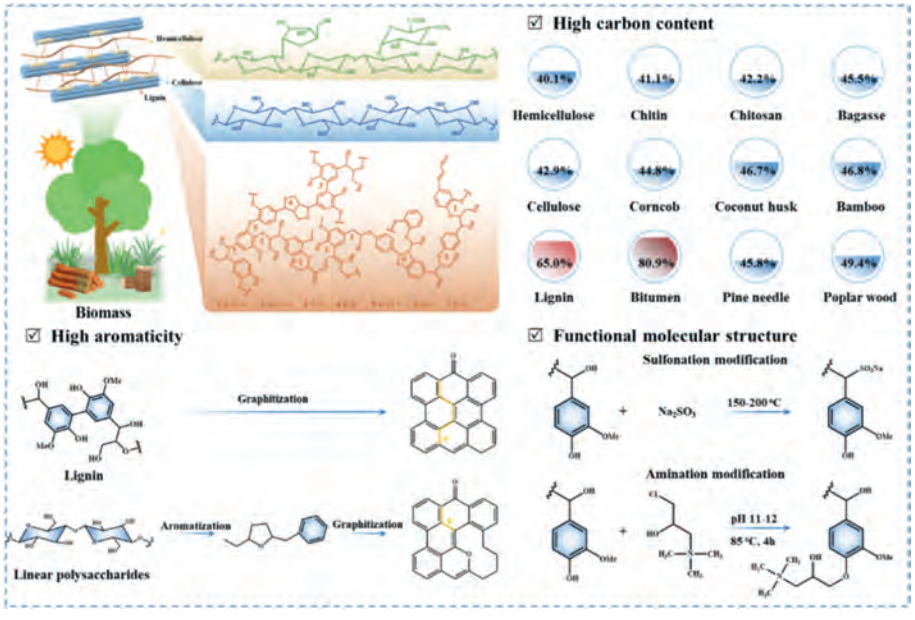


Fig. 2. Schematic diagram of biomass structure and the advantages of lignin as a carbon source to prepare porous carbons.

Table 1
Pore structure parameters of lignin-derived porous carbons using lignin precursor by different methods.

Methods	Raw materials	Temp (°C)	Mass ratio	Specific surface area (m^2/g)	Total pore volume (cm^3/g)	Pore volume (cm^3/g)		Ref.
						Micropores	Mesopores	
Direct carbonization	Enzymatic hydrolysis lignin	600	–	184	0.11	–	–	[53]
		800	–	536	0.22	–	–	
		1000	–	282	0.13	–	–	
		1200	–	4	0.01	–	–	
		1400	–	1	0.01	–	–	
		1600	–	4	0.01	–	–	
	Alkali lignin	800	–	405	0.21	0.15	0.06	[56]
	Sodium lignosulfonate	700	–	366	0.13	0.09	0.04	[58]
		800	–	574	0.35	0.18	0.17	
		900	–	500	0.28	0.15	0.13	
	Calcium lignosulfonate	700	–	599	0.28	0.19	0.08	[59]
		800	–	542	0.27	0.16	0.11	
		900	–	437	0.30	0.10	0.19	
Chemical activation	Lignin sulfate/KOH	600	1:1	1605	0.69	0.54	–	[60]
			1:3	2049	0.95	0.70	–	
			1:5	501	0.21	0.17	–	
	Alkali lignin/KOH	700	1:3	1495	0.61	0.40	0.20	[61]
		800		1009	0.39	0.31	0.08	
		900		2316	1.47	0.36	1.11	
	Alkali lignin/K_2CO_3	700	1:3	1052	0.39	0.34	0.03	[61]
		800		1434	0.54	0.47	0.04	
		900		1800	0.70	0.57	0.11	
	Lignin sulfate/NaOH	600	1:1	510	0.21	0.16	–	[60]
			1:3	1626	0.67	0.63	–	
			1:5	236	0.12	0.08	–	
Hard and soft template	Alkali lignin/CaO	600	2:1	699	0.39	0.18	0.21	[62]
		700		734	0.47	0.17	0.30	
		800		849	0.60	0.17	0.43	
		900		807	0.53	0.18	0.35	
		1000		852	0.61	0.15	0.46	
	Enzymatic hydrolysis of lignin/MgO	600	2:1	827	0.69	–	–	[63]
	Alkali lignin/MgO	1000	10:1	85	0.10	–	0.07	[64]
	Alkali lignin/SiO_2	700	1:1	114	0.21	0.04	0.04	[66]
	Alkali lignin/SiO_2	600	1:1	1107	2.35	0.29	2.06	[65]
	Lignin sulfonates/SiO_2	700	1:1	283	0.18	0.11	–	[67]
	Alkali lignin/F127	1000	10:16	59	0.09	–	0.07	[64]
	Lignin sulfonates/F127	700	10:1	176	0.13	0.07	–	[67]
Carbonate and oxalate activations	Enzymatic hydrolysis of lignin/$ZnCO_3$	400	1:1	51	0.08	0.02	0.01	[70]
		500		109	0.11	0.02	0.06	
		600		531	0.42	0.06	0.28	
		700		677	0.78	0.05	0.66	
	Alkali lignin/$CaCO_3$	600	1:5	449	0.64	0.13	0.51	[71]
		700		837	2.87	0.11	2.76	
		800		830	1.54	0.07	1.47	
		900		455	0.66	0.06	0.60	
	Lignin sulfonates/$MgCO_3$	800	1:1	587	0.81	0.01	0.40	[72]
	Sodium lignosulfonate/ZnC_2O_4	650	1:1	585	0.87	0.06	0.81	[73]
			1:2	1069	1.38	0.18	1.20	
			1:3	872	1.13	0.12	1.01	
		550	1:2	232	0.31	0.01	0.31	
		750		1300	2.03	0.07	1.96	
	Sodium lignosulfonate/CaC_2O_4	600	1:2	491	0.49	0.17	0.23	[74]
		700		1029	0.75	0.35	0.32	
		800		1176	0.87	0.41	0.36	
	Sodium lignosulfonate/MgC_2O_4	700	1:2	473	0.26	0.13	0.07	[31]

2.1. Chemical activation

Chemical activation refers to the strong etching of chemical reagents on graphene nanocrystals or microcrystals to construct developed porous structures. Common chemical activators mainly include alkali metal reagents, $ZnCl_2$ and H_3PO_4, among which potassium reagents (KOH, K_2CO_3, *etc.*), and sodium reagents (NaOH, *etc.*) are mainly studied due to their high activation efficiency and excellent universality.

As shown in Table 1, the optimal mass ratios of lignin/KOH, lignin/K_2CO_3, and lignin/NaOH to prepare the porous carbons with the highest specific surface area and pore volume are 1:3 and the optimal temperature is 800 °C. Lignin-derived porous carbons prepared by NaOH activation have lower specific surface areas and total pore volumes than those prepared by KOH activation [60,61]. Therefore, KOH activation is useful for preparing lignin-derived porous carbons with high specific surface areas and pore volume.

2.2. Template methods

The template methods refer to the space occupancy role of template reagents in the carbon matrixes during the carbonization process, and the porous structures are constructed after removing inorganic oxides. The template methods can be divided into hard template and soft template methods.

The common hard templates mainly include nano-SiO_2, CaO, and MgO. As shown in Table 1, due to high surface energy, the nano-sized hard templates tend to agglomerate through van der

Waals forces, hydrogen bonding, or electrostatic interaction. The lignin-derived porous carbons prepared by CaO and MgO templates have low specific surface areas, total pore volumes, and mesoporosities [62–64]. Based on the force regulation between lignin and SiO_2 templates, the uniform mixing of hard template and lignin can be achieved to prepare lignin-derived porous carbons with high porosity [65–67].

The common soft templates include surfactants (F127, *etc.*) and block copolymers (P123, *etc.*). As shown in Table 1, the strong interaction between lignin molecules and soft templates hinders the self-assembly of soft templates to form micelles and lamellar or hexagonal mesophases, making it difficult to orderly control the pore structure of lignin-derived porous carbons. Consequently, the specific surface areas and total pore volumes of the prepared lignin-derived porous carbons are lower than 200 m^2/g and 0.13 cm^3/g, respectively [64,67]. However, the micelles formed by lignin and soft templates can assemble on the surface of structure-directing agents to prepare lignin-derived porous carbons with accordion-like and flower-shaped morphologies [68,69].

Carbonate and oxalate activations are a new type of method that combines physical activation and template effects to prepare lignin-derived porous carbons, because they could decompose into CO_2 and metal oxides during the carbonization process.

As shown in Table 1, the metal carbonates have weak activation effects and mainly act as templates. The pore structures of the prepared lignin-derived porous carbons are dominated by mesopores [70–72]. The ratio of activation and template effect of metal oxalates can be adjusted. The sodium lignosulfonate-derived porous carbons prepared by ZnC_2O_4 activation exhibit the highest specific surface area of 1069 m^2/g, total pore volume of 1.38 cm^3/g and a mesoporosity of 98.4%, when the mass ratio of sodium lignosulfonate to ZnC_2O_4 and the temperature are 1:2 and 650 °C, respectively [73]. Compared with the simultaneous release of CO and CO_2 by ZnC_2O_4 decomposition, MgC_2O_4 decomposition weakly-staged releases CO and CO_2, and CaC_2O_4 decomposition respectively releases CO and CO_2, which could construct micropore-dominated and uniformly-distributed hierarchical porous structures, respectively [31,74].

3. Lignin-derived porous carbon cathodes for ZIHCs

3.1. Pore regulation of lignin-derived porous carbon cathodes

The charge storage mechanism is key to the pore regulation of porous carbons. As shown in Fig. 3a, during the charge and discharge processes of ZIHCs, the $Zn_4SO_4(OH)_6{\cdot}5H_2O$ is generated at low potentials and disappears at high potentials [75]. The generation of $Zn_4SO_4(OH)_6{\cdot}5H_2O$ can be ascribed to the co-adsorption of Zn^{2+} and H^+ ions at low potentials. The electrochemical adsorption of H^+ ions forms a dynamic local alkaline environment near the electrode surface, where OH^- anions strongly coordinate with Zn^{2+} ions to generate $Zn_4SO_4(OH)_6{\cdot}5H_2O$. The adsorption process of Zn^{2+} and H^+ ions in the pore structure is schematically illustrated in Fig. 3b [76].

The ionic radius of Zn^{2+} ions (0.074 nm) is greater than that of H^+ ions (0.0087 nm). Therefore, the adsorption of Zn^{2+} ions is more important for the pore structure. Zn^{2+} ions generally exist in aqueous electrolytes in the form of hydrated Zn^{2+} ($Zn(H_2O)_6^{2+}$) ions. $Zn(H_2O)_6^{2+}$ ions are crucial charge carriers in ZIHCs [22,76–78]. The micropores, mesopores, and macropores in the pore structure play the roles of storage, transport, and reservoir, respectively. The influence of $Zn(H_2O)_6^{2+}$ ion storage by micropores on the capacitive performance is of vital importance. As shown in Fig. 4a, when the micropore size is too low, $Zn(H_2O)_6^{2+}$ ions enter pore channels with distortion, resulting in low kinetics and low surface area utilization [79]. When the micropore size is too large,

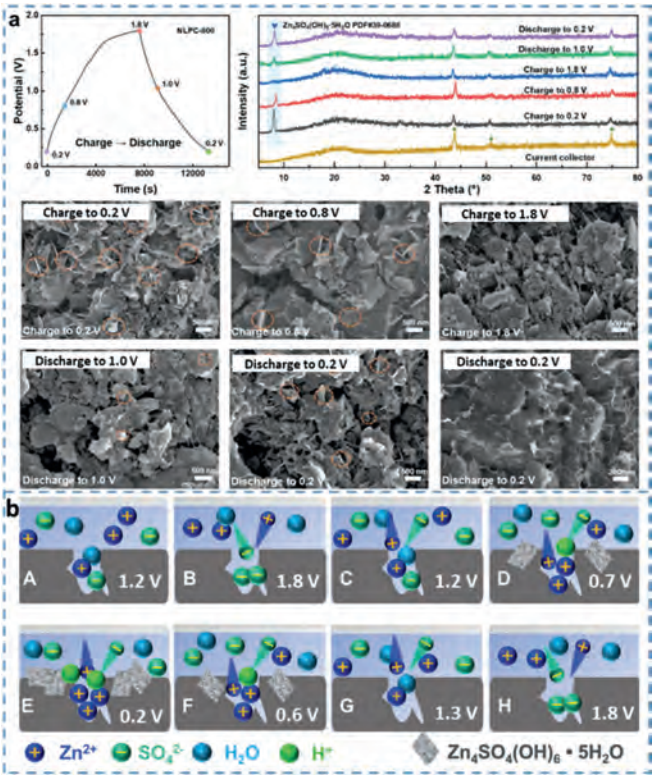


Fig. 3. (a) *Ex situ* XRD patterns and SEM images of lignin-derived porous carbon cathodes under different potentials. Reproduced with permission [75]. Copyright 2025, Elsevier. (b) Schematic diagram of the charge storage mechanism in porous structures. Reproduced with permission [76]. Copyright 2022, Wiley-VCH.

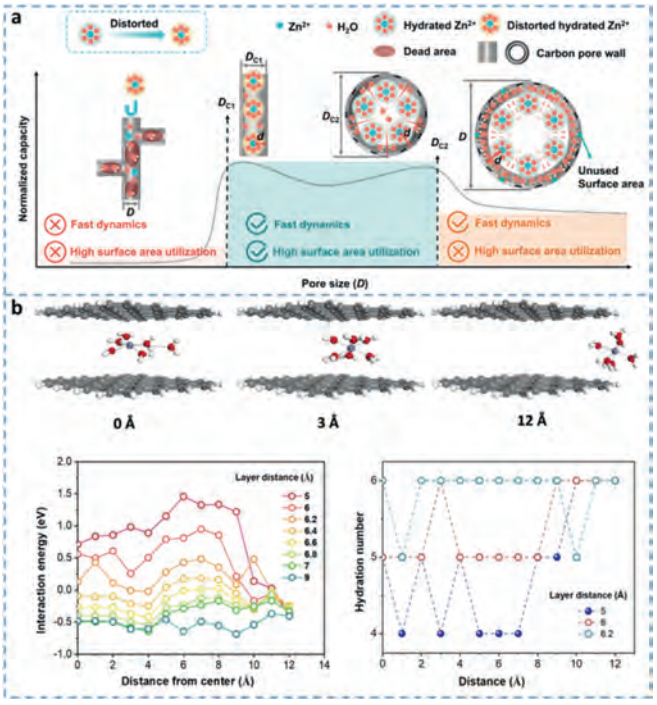


Fig. 4. (a) Schematic diagram of the relationship between pore size and kinetics. Reproduced with permission [79]. Copyright 2024, Royal Society of Chemistry. (b) Molecular dynamics simulations of the intercalation process of $Zn(H_2O)_6^{2+}$ ion. Reproduced with permission [80]. Copyright 2022, Elsevier.

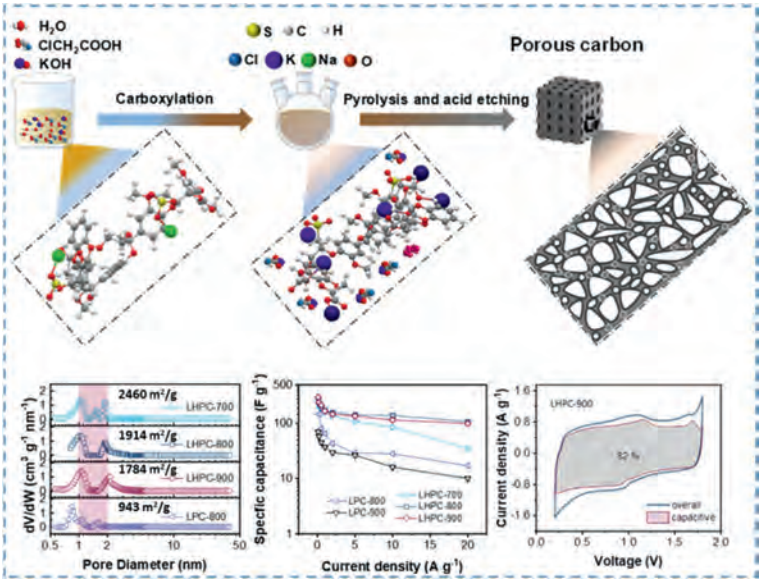


Fig. 5. Preparation of lignin-derived porous carbons by multi-scale potassium salt activation. Reproduced with permission [85]. Copyright 2022, Elsevier.

the kinetics are improved, but the surface area utilization is still low. The appropriate micropore size facilitates the rapid transport of $Zn(H_2O)_6^{2+}$ ions, contributing to fast kinetics and high surface area utilization.

Many works have been conducted to explore the appropriate micropore size. As shown in Fig. 4b, through first-principles simulation calculations, Zhang *et al.* found that the $Zn(H_2O)_6^{2+}$ ions were difficult to enter the micropores with a size of 0.5 nm due to high intercalation energy [80]. Even under an intercalated state, $Zn(H_2O)_6^{2+}$ ions would lose one or two water molecules. With the increase in graphene distance, the intercalation energy decreased significantly. When the pore size was larger than 0.68 nm, the entry of $Zn(H_2O)_6^{2+}$ ions was quite smooth. There exists another viewpoint on the most appropriate micropore size for storing $Zn(H_2O)_6^{2+}$ ions. The diameter of $Zn(H_2O)_6^{2+}$ ion is 0.86 nm. The density functional theory (DFT) simulation calculations indicate that the intercalation energy significantly decreases as micropore size increases above 0.86 nm [22,23]. Therefore, they believe that the micropores with the sizes larger than 0.86 nm are suitable for storing $Zn(H_2O)_6^{2+}$ ions. Interestingly, the recent studies have demonstrated that microporous carbon cathodes also exhibit excellent specific capacitance and rate performance [32,81–83]. Simultaneously, it has been demonstrated that large micropores with the sizes of 0.9–2 nm can serve as transport channels [77]. However, the micropores with the sizes of 0.86–0.90 nm are insufficient to store a large number of $Zn(H_2O)_6^{2+}$ ions. Therefore, the first viewpoint that micropores with the sizes larger than 0.68 nm could effectively store $Zn(H_2O)_6^{2+}$ ions, has higher reliability.

The lignin-derived porous carbons with a hierarchical micropore-small mesopore structure could exhibit good capacitive performance. Zhang *et al.* prepared lignin-derived porous carbons from alkali lignin by KOH activation at 800 °C, which had a specific surface area of 1483 m^2/g, microporosity of 74 % and mesoporosity of 25 % [84]. The pore structure was dominated by 0.6–1.3 nm micropores and 2–3 nm mesopores. The prepared lignin-derived hierarchical porous carbons (LHPC) delivered the specific capacitances of 261 and 135 F/g at 0.1 and 20 A/g, respectively. The assembled LHPC//Zn ZIHCs delivered the highest energy density of 116 Wh/kg. As shown in Fig. 5, Zhao *et al.* prepared LHPCs with different porous structures by a temperature-controlled multi-scale potassium salt activation method [85]. Without potassium activation, the lignin-derived porous carbons prepared at 800 °C (LPC-800) had 0.85, 1.05, and 1.6 nm micropores, exhibiting a low capacitance of 200 F/g at 0.1 A/g and poor rate performance (20 F/g at 20 A/g). The LHPCs prepared at 700 °C (LHPC-700) with 1, 1.5, and 1.85 nm micropores showed a higher capacitance of 256 F/g at 0.1 A/g and improved rate performance, which indicates that 1–2 nm micropores could transport $Zn(H_2O)_6^{2+}$ ions. The LHPCs prepared at 800 °C (LHPC-800) with 1 and 1.85 nm micropores and 2–3 nm mesopores showed similar capacitance to LHPC-700, while having an excellent rate performance. This phenomenon suggests that 2–3 nm mesopores could significantly promote rapid diffusion kinetics. The LHPCs prepared at 900 °C (LHPC-900) had a similar pore distribution to LHPC-800, while the microporosity was relatively higher, exhibiting a high capacitance of 298 F/g at 0.1 A/g and slightly deteriorated rate performance. The contribution of the electric double layer to the total capacitance was 82 % at 2 mV/s. The ZIHCs assembled using LHPC-900 in a 1 mol/L $ZnSO_4$ electrolyte had a high energy density of 135 Wh/kg at a power density of 101 W/kg. Therefore, the lignin-derived porous carbons with hierarchical micropore-small mesopore structure could deliver a superior capacitive performance than those with microporous structures. The ratio of micropores to small mesopores in hierarchical micropore-small mesopore structure significantly affects the capacitive performance of lignin-derived porous carbons.

In addition to potassium activation, sodium activation has also been studied to regulate the pore structure of lignin-derived porous carbons. As shown in Fig. 6, Yi *et al.* prepared alkali lignin-derived porous carbons (BLCs) by NaOH activation at 600–900 °C [86]. The BLCs prepared at 600–900 °C showed 0–1 nm micropore-dominated porous structures. The BLCs prepared at 800 °C (BLC-800) with high micropore volume exhibited the highest specific capacitance of 244 F/g at 0.1 A/g, and the best rate performance of 150 F/g at 20 A/g. Electrochemical analysis revealed that the contribution of the electric double layer to capacitance was only 45 % at 5 mV/s. The assembled BLC-800//Zn showed high energy densities of 84.6 Wh/kg at 359 W/kg and 9900 W/kg at 20.4 Wh/kg. As the cathode materials for ZIHCs, the lignin-derived porous carbons prepared by sodium activation show lower capacitive performance than those prepared by potassium activation. This result can be attributed to that sodium activation constructs a porous structure dominated by small micropores (<1 nm), while potassium activation constructs a hierarchical micropore-small mesopore structure

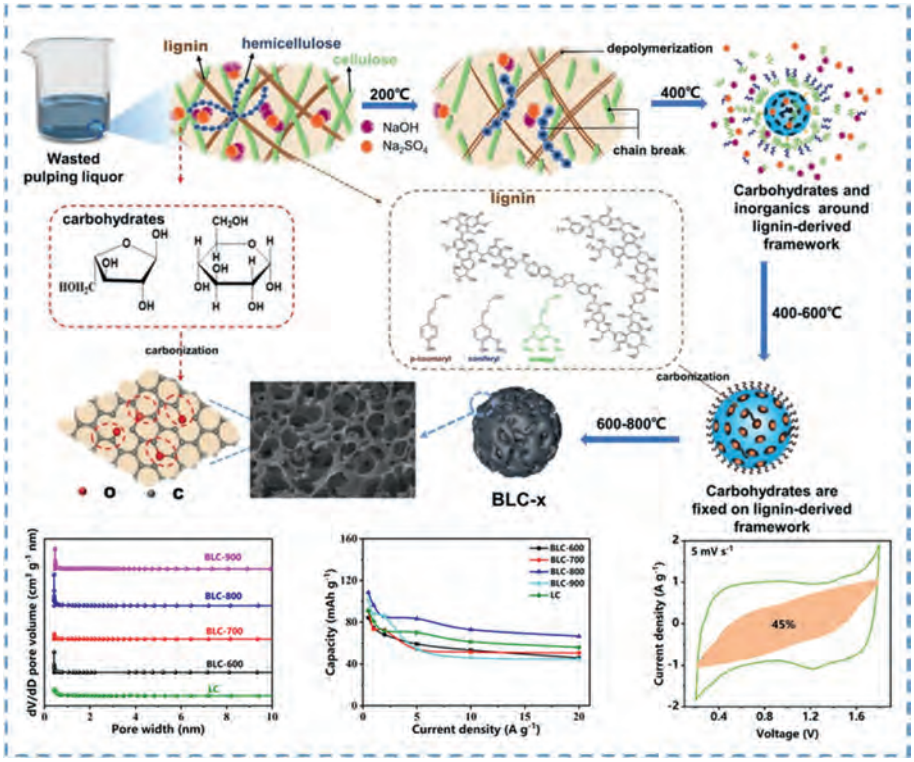


Fig. 6. Preparation of lignin-derived porous carbons by NaOH activation. Reproduced with permission [86]. Copyright 2024, Elsevier.

or a porous structure with the coexistence of small and large micropores (1–2 nm).

Mesopore plays a key role in transporting $Zn(H_2O)_6^{2+}$ ions. Further understanding the effect of mesopores on capacitive performance is of great significance to regulate the pore structure of lignin-derived porous carbons. Zhang *et al.* prepared LPCs with different mesoporosities by $CaCO_3$ activation at 600–900 °C [62]. As the carbonization temperature increased, the mesoporosities of LPCs first increased and then decreased, reaching the highest at 800 °C. The LPCs prepared at 800 °C (LPC-800) showed a specific surface area of 849 m^2/g and the highest mesoporosity of 71.7 %, exhibiting the best rate performance. The LPCs prepared at 700 °C (LPC-700) and 900 °C (LPC-900) had the same mesoporosities, showing similar rate performance. Due to the lowest mesoporosity, the LPCs prepared at 600 °C (LPC-600) exhibited the poorest rate performance. Therefore, the mesoporosity is generally positively correlated with the rate performance. Besides, the capacitance is generally positively correlated with the microporosity. With the decrease in the mesoporosity of LPCs, the capacitance became smaller. As shown in Fig. 7, Zhu *et al.* prepared LPCs by nano-$CaCO_3$ activation at 600–900 °C to further study the effect of higher mesoporosity on rate performance [71]. The LPCs prepared at 800 °C (LPC-800) with a specific surface area of 830 m^2/g had a mesoporosity of 94.8 %, higher than the LPCs prepared at 600 °C (LPC-600) (80.3 %). LPC-800 showed a higher rate performance than LPC-600 due to the higher mesoporosity, while its capacitance was relatively lower (157 F/g at 0.1 A/g), attributed to the low microporosity. Therefore, under the condition of high mesoporosity, the further increase in mesoporosity is also beneficial for improving rate performance. However, the LPCs prepared at 700 °C (LPC-700) and 900 °C with the highest mesoporosities of 96.1 % and 90.3 % possessed inferior rate performance, which is mainly limited to low microporosity and micropore volume. The contribution of the electric double layer to the capacitance was up to 85 % at 2 mV/s. The assembled LPC-800//Zn ZIHCs exhibited an energy density of approximately 60 Wh/kg.

To summarize, the contribution of the electric double layer to the capacitance is the highest at high mesoporosity, followed by that at medium mesoporosity, and finally at low mesoporosity. Therefore, the high proportion of mesopores could effectively enhance the utilization of micropores. However, the low micropore volume could cause poor ability to store $Zn(H_2O)_6^{2+}$ ions, resulting in a decrease in capacitive performance.

A rational hierarchical porous structure with an appropriate micropore-mesopore distribution should have optimal capacitive performance. The combination of chemical activation and template is naturally thought of for the preparation of high-performance lignin-derived hierarchical porous carbons (LHPCs). As shown in Fig. 8, Fan *et al.* [87] prepared NSLHPC from enzymatic hydrolysis lignin by combining KOH/KSCN activation and MgO template at 800 °C. The LPC prepared by KOH activation had a hierarchical porous structure with low mesoporosity, exhibiting the second-highest specific capacitance, but the rate performance was poor. The NSLPC prepared by KSCN activation and MgO template had a hierarchical porous structure with higher mesoporosity, showing a lower specific capacitance and higher rate performance. The lignin-derived carbon (LC) prepared by MgO template had a hierarchical porous structure with the highest mesoporosity, exhibiting the poorest capacitance and rate performance. NSLHPC exhibited a specific surface area of 2705 m^2/g with suitable microporosity and mesoporosity of 14.1 % and 64.5 %, respectively. The pore size distribution was located at 0.6/1.2 nm micropores, 2–30 nm mesopores and 50–100 nm macropores. NSLHPC displayed the excellent capacitances of 295 F/g at 0.2 A/g and 147 F/g at 10 A/g. The contribution of the electric double layer to the capacitance was 54 % at 2 mV/s. The assembled NSLHPC//Zn ZIHCs exhibited a high energy density of 104.9 Wh/kg at a power density of 160.6 W/kg.

3.2. Surface modification of lignin-derived porous carbon cathodes

The modification of heteroatoms on the surface of lignin-derived porous carbons can regulate physicochemical properties to

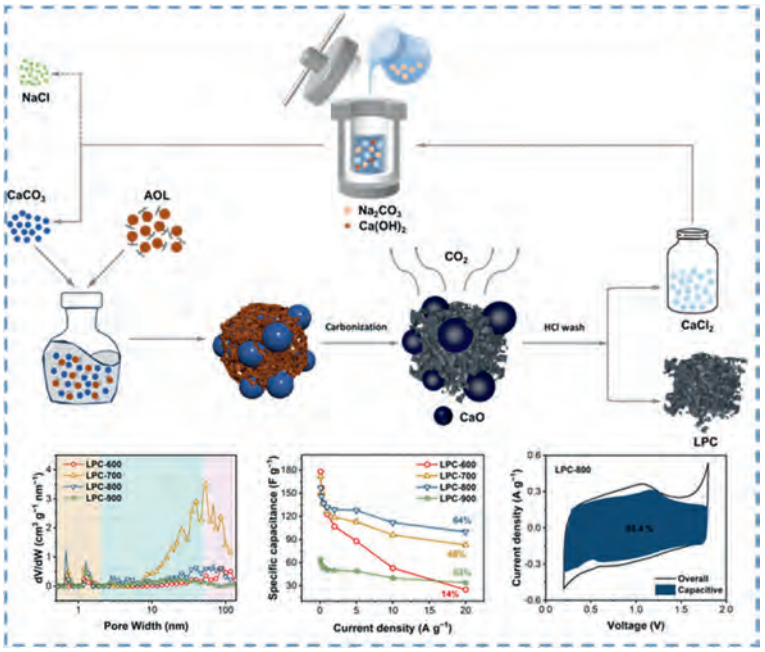


Fig. 7. Preparation of lignin-derived porous carbons by nano $CaCO_3$ activation. Reproduced with permission [71]. Copyright 2024, Royal Society of Chemistry.

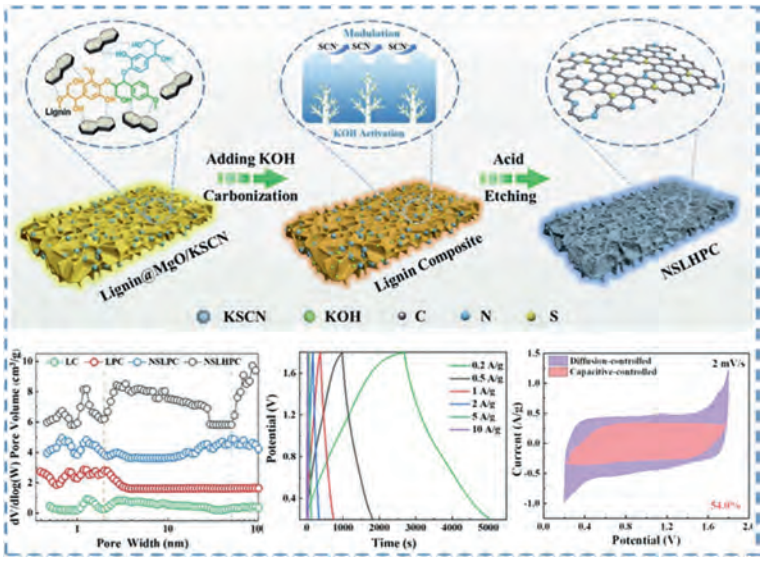


Fig. 8. Preparation of lignin-derived hierarchical porous carbons by KSCN/KOH activation combining with MgO template. Reproduced with permission [87]. Copyright 2024, Elsevier.

improve capacitive performance, such as changing electron density distribution and interfacial hydrophobicity and enhancing pseudocapacitive contributions.

Nitrogen (N) atom is the most extensively studied doped atoms for porous carbon cathode materials owing to the following superiorities. (1) N can provide additional electrons to enhance electron transport capability, *i.e.*, pyridinic N (N-6) contributing one p-electron to the six-membered conjugated system and pyrrolic N (N-5) providing two p-electrons to the five-membered conjugated system. (2) The electronegativity of the N atom (-3.04) is higher than that of the carbon (C) atom (-2.55), which can enhance the interaction with Zn^{2+} ions. Meanwhile, the N-5 and N-6, collectively classified as edge N, can reversibly adsorb Zn^{2+} ions through redox reactions, which achieves high capacitance. (3) N has the function of enhancing hydrophobicity and increasing interfacial compatibility between electrodes and electrolytes.

As shown in Fig. 9a, our research group innovatively utilized alkali lignin extracted from eucalyptus as a raw material, and prepared edge N-doped hierarchical porous carbons (ENHPCs) by co-pyrolyzing lignin with K_2CO_3 and melamine at 800 °C [88]. KOCN generated by K_2CO_3 reacting with cyano groups (–CN), coupling with K_2CO_3 activation, constructed a large specific surface area. KCN *in-situ* generated by KOCN etching carbon atoms, played a template role in constructing centralized mesopores. Edge N skeleton was formed by g-C_3N_4 losing –CN, and then *in-situ* integrated into porous carbon skeleton, achieving accurate edge N dopant. The ENHPCs prepared at a melamine/lignin mass ratio of 0.5 (ENHPC-0.5) had a specific surface area of 3122 m^2/g, a mesoporosity of 60.5 % and an edge N content of 1.9 at%, exhibiting outstanding capacitive performance (350 F/g at 0.1 A/g and 129 F/g at 20 A/g), which exceeds the performance of commercial YP-50F activated carbons. Due to the efficient doping of N atoms, the contribution

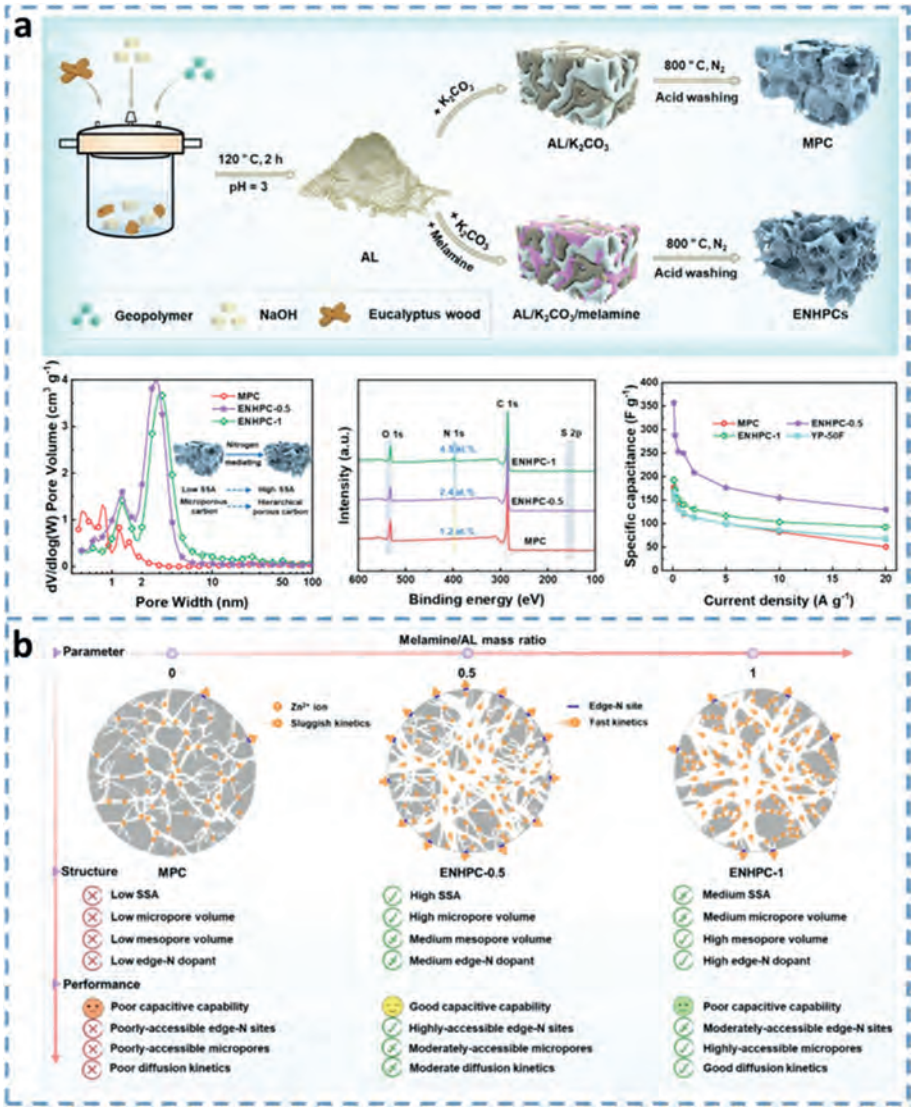


Fig. 9. (a) Preparation of edge nitrogen-doped lignin-derived porous carbons through the co-pyrolysis of lignin, K_2CO_3 and melamine. (b) Process parameter-structure-performance relationships. Reproduced with permission [88]. Copyright 2025, Elsevier.

of the electric double layer to the capacitance was only 22.1 % at 2 mV/s. The assembled ENHPC-0.5//Zn ZIHCs exhibited 120 Wh/kg at 80 W/kg.

We also established the relationship of process parameter-structure-performance, as shown in Fig. 9b The microporous carbons prepared without melamine addition show a poor capacitive performance due to the poorly accessible micropores and poor diffusion kinetics by the lack of mesopore volume and poorly accessible edge-N sites by low specific surface area (SSA). Although medium mesopore volume could not completely activate high micropore volume, high SSA could activate medium edge-N sites, endowing a good capacitive performance of ENHPC-0.5. In contrast, high mesopore volume could activate medium active micropore volume, while medium SSA could not fully activate high edge-N sites. Although mesopore structure with larger mesopore size and mesopore volume provides good diffusion kinetics, the ENHPCs prepared at a melamine/lignin mass ratio of 1 (ENHPC-1) exhibit poor capacitive performance. Therefore, if edge N can be maximally utilized, the capacitance would be greatly improved.

The mechanism that edge N stores Zn^{2+} ions has been deeply explored by theoretical simulation calculations and *ex-situ* XPS characterization. As shown in Fig. 10a, the adsorption energies of N-6 and N-5 are lower than graphene (G) and graphitic N (N-Q), which could boost the chemical adsorption of Zn to enhance interfacial pseudocapacitance. As shown in Fig. 10b, the edge-N ratio of ENHPC-0.5 fluctuates within a small range of 69.2 %–71.0 % during the discharging/charging processes, indicating the excellent stability of pseudocapacitive adsorption by edge N. The N-6 ratio increases in the charging process and decreases in the discharging process. The change in N-5 ratio is opposite to that of N-6 ratio. Therefore, edge N has excellent electrochemical reversibility. The pseudocapacitive behavior of edge N mainly relies on the strong electronegative N-6 adsorbing Zn^{2+} ions.

The quantitative relationship of micropore and edge-N with capacitive performance is an important reference for the development of high-performance lignin-derived porous carbons. As shown in Fig. 11a, our research group further analyzed the structure-performance relationship between micropore/edge-N and capacitance through regulating the temperature of the co-pyrolysis of lignin, K_2CO_3 and melamine [75]. As illustrated in Fig. 11b, as the carbonization temperature increases from 500 °C to 900 °C, the edge-N/specific surface area (SSA) ratio negatively-gradient decreases from 3.6 at% mg/m^2 to 0.3 at% mg/m^2, and the micropore/mesopore (V_{micro}/V_{meso}) ratio negatively-gradient decreases

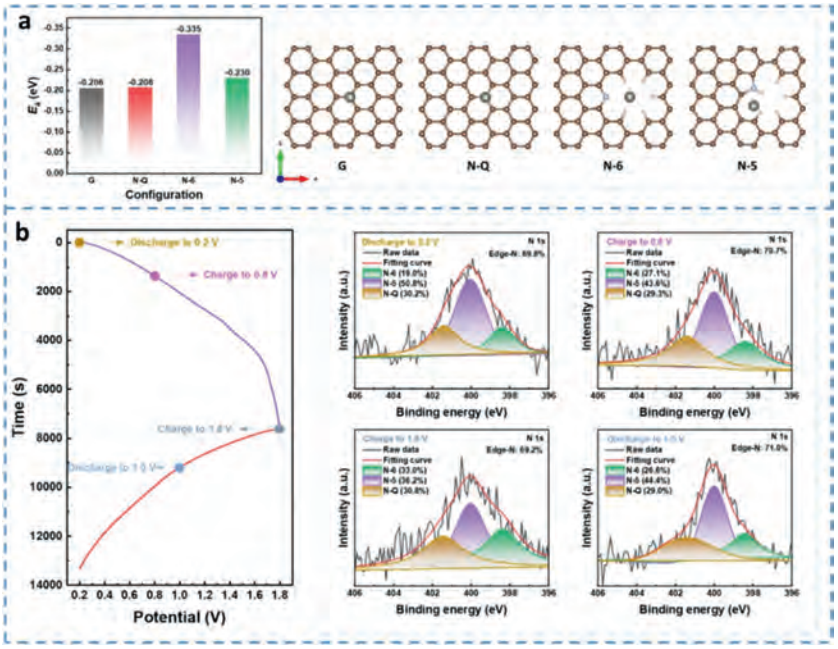


Fig. 10. (a) First-principles calculations of Zn adsorption on different graphene configurations. (b) *Ex-situ* N 1s XPS characterization. Reproduced with permission [88]. Copyright 2025, Elsevier.

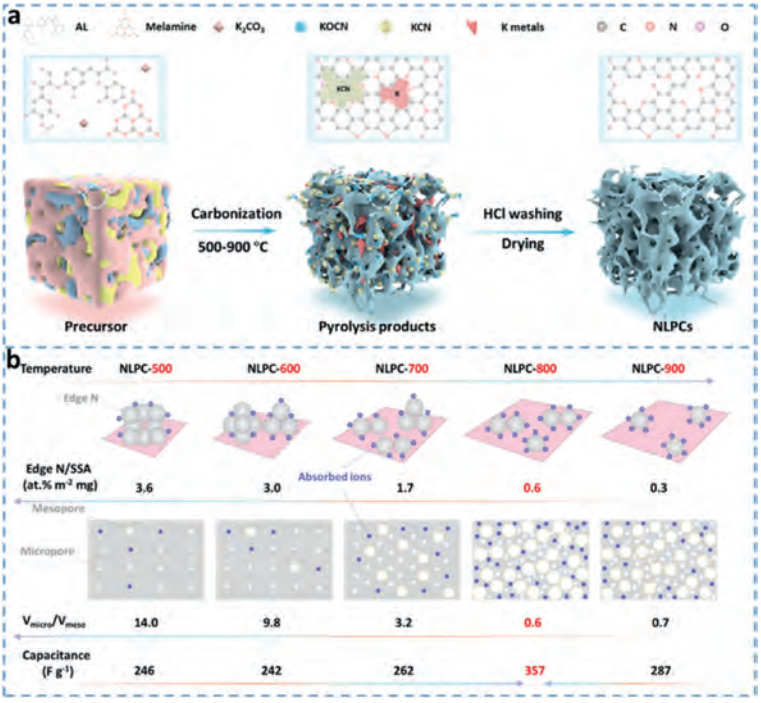


Fig. 11. (a) Schematic diagram for the preparation of N-doped lignin-derived porous carbons (NLPCs). (b) Relationship between edge nitrogen/surface area ratio and micropore/mesopore ratio with capacitive performance. Reproduced with permission [75]. Copyright 2025, Elsevier.

from 14.0 to 0.6. The decrease in the edge-N/SSA ratio effectively exposes edge-N sites to improve their accessibility, enhancing the pseudocapacitive capability to store Zn^{2+} ions. The decrease in the V_{micro}/V_{meso} ratio enhances the accessibility of micropores, providing a greater amount of Zn^{2+} ion adsorption sites. At the optimal edge-N/SSA ratio of 0.6 at% m^{-2} mg and the lowest V_{micro}/V_{meso} ratio of 0.6, the specific capacitance and rate performance of the N-doped lignin-derived porous carbons prepared at 800 °C (NLPC-800) are the best, displaying capacitances of 357 F/g at 0.1 A/g and 126 F/g at 20 A/g. The NLPC-800//Zn ZIHCs displayed high energy densities of 126 and 25 Wh/kg at power densities of 80 and 9677 W/kg, respectively.

O is main element in the carbon precursors and lignin-derived porous carbons, which is only second to C. O atoms are difficult to be completely removed in the carbonization process due to the confinement of complex linkages, and exist in carbon materials. Therefore, O atoms are also second to C atoms in carbon materials. O dopants can generate pseudocapacitive interactions with Zn^{2+} ions. However, only a specific O configuration can pseudocapacitively adsorb Zn^{2+} ions reversibly. As shown in Fig. 12a, it

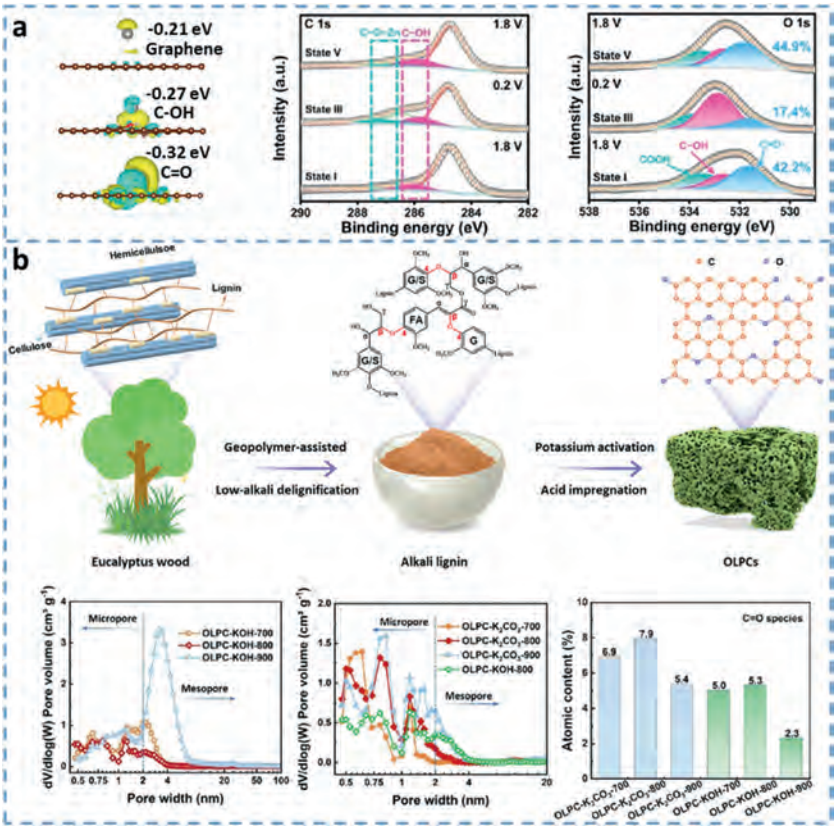


Fig. 12. (a) Adsorption energies of O configurations toward Zn atom and *ex-situ* C 1s/O 1s spectra. Reproduced with permission [89]. Copyright 2022, American Chemical Society. Reproduced with permission [90]. Copyright 2023, Elsevier. (b) Preparation of oxygen-rich lignin-derived porous carbons by KOH and K_2CO_3 activations. Reproduced with permission [61]. Copyright 2024, KeAi.

has been widely reported that the carbonyl group (C=O) is an active oxygen configuration to adsorb Zn^{2+} ions due to its higher adsorption energy towards Zn^{2+} ion than graphene (G) and hydroxyl group (-OH) and the reversible reaction with Zn^{2+} ions through $C{=}O + Zn^{2+} \rightarrow C\text{-}O\text{-}Zn$ [89,90]. As shown in Fig. 12b, Liang *et al.* prepared O-enriched alkali lignin-derived porous carbons (OLPCs) by KOH activation and K_2CO_3 activation at 700–900 °C, respectively [61]. Compared with KOH activation, K_2CO_3 activation was more effective in constructing active C=O species. KOH activation mainly constructed hierarchical microporous-mesoporous structures, while K_2CO_3 activation mainly constructed microporous structures. The OLPCs prepared by KOH and K_2CO_3 activations at 800 °C had the highest C=O content (5.3/8.0 at%) and microporosity (78.4 %/87.7 %). The capacitance of OLPCs prepared by K_2CO_3 activation (256 F/g at 0.1 A/g) was better than that prepared by KOH activation (224 F/g at 0.1 A/g), attributed to the high C=O content providing high pseudocapacitance. The assembled ZIHCs delivered the energy densities of 91/37 Wh/kg at the power densities of 80/16,000 W/kg. Zhang *et al.* first used a dual-activation method of $CaCl_2$ and K_2CO_3 (the mass ratio of $CaCl_2$ and K_2CO_3 to lignin is 4) to prepare lignin-derived porous carbons (LCK4) at 850 °C and then oxidized them in nitric acid at 60 °C for 3 h to prepare O-enriched LCK (OLCK4) [91]. The LCK4 had a specific surface area of 984 m^2/g, which was close to OLCK4 (1056 m^2/g). The O content of LCK4 (5.4 at%) was lower than that of OLCK4 (18.8 at%). Therefore, OLCK4 exhibited higher specific capacitances of 274 F/g at 0.3 A/g and 109 F/g at 20 A/g than LCK4 (216.9 F/g at 0.3 A/g and 157.1 F/g at 7 A/g). The OLCK4//Zn ZIHCs delivered an energy density of up to 94.3 Wh/kg. Although the increase in O content can improve capacitance, the excessive O dopants can damage the π-conjugate structure of the porous carbon skeleton, reducing conductivity and lowering capacitive performance. Therefore, the positive transformation of oxygen into an efficient C=O group is particularly significant for the preparation of high-performance O-rich lignin-derived porous carbons.

The dopants of N and O have a positive effect on the capacitance of lignin-derived porous carbons. The theoretical simulation studies have demonstrated that the co-dopants of N and O can produce synergistic effects in influencing the capacitive performance. As shown in Fig. 13, based on density functional theory (DFT) calculations, He *et al.* found that when the C=O and N-6 or N-5 were simultaneously introduced into the graphene surface, the adsorption of Zn^{2+} ion was significantly enhanced [92]. When N-6 or N-5 was adjacent to C=O, the adsorption energies respectively reached -0.689 and -1.432 eV, indicating that N-6 and N-5 dopants could effectively improve the chemisorption of C=O towards Zn^{2+} ions. In addition, when the N-6 or N-5 and C=O were distributed in alternate positions, the adsorption energies further decreased to -0.867 and -1.657 eV. Combining with Bader charge analysis, the synergistic effects of N-6 and N-5 and C=O on Zn^{2+} ion adsorption can be divided into the following two aspects: (1) The N-6 and N-5 adjacent to the carbonyl groups could greatly reduce the adsorption energy between C=O and Zn^{2+} ions by inducing charge delocalization of carbonyl groups; (2) The C=O could further chemically adsorb Zn^{2+} by bonding with the alternate N-6 and N-5 to form N–Zn–O bonds. Xue *et al.* prepared N,O-doped lignin-derived porous carbons from alkali lignin by the co-pyrolysis with $K_2C_2O_4$ and urea at 700–900 °C [93]. Through the temperature optimization, the N,O-doped lignin-derived porous carbons prepared at 800 °C (AL-KNPC-800) had a specific surface area of 1949 m^2/g, a N content of 1.64 at%, and an O content of 8.42 at%, exhibiting the highest specific capacitance of 360 F/g at 0.1 A/g and rate per-

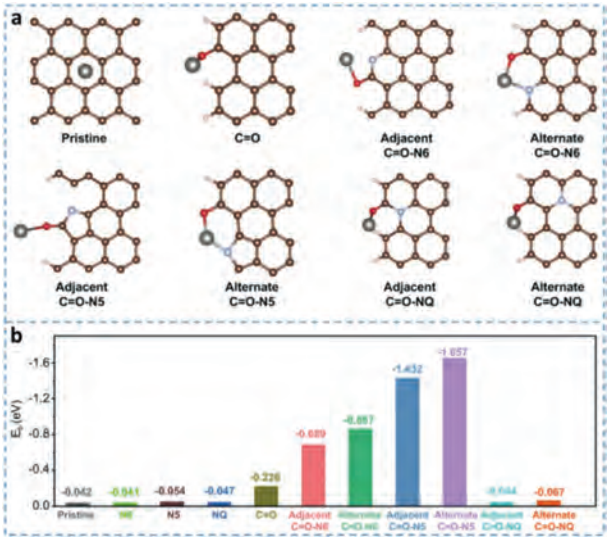


Fig. 13. (a) Adsorption model of Zn atom on pristine graphene and different functionalized graphenes. (b) The corresponding adsorption energies of Zn atom on pristine graphene and different functionalized graphene. Reproduced with permission [92]. Copyright 2022, Springer Nature.

formance of 211 F/g at 20 A/g. The AL-KNPC-800//Zn ZIHCs delivered the energy densities of 127 Wh/kg at 79 W/kg and 54 Wh/kg at 52 W/kg.

Sulfur (S) is located in the sixth major group of the periodic table. The electronegativity of S atom (-2.58) is lower than C atom (-2.55), which can be used as an electron donor. The introduction of S increases electron density and surface polarization, and promotes charge transfer. The S dopant can increase carbon spin density and structural defects. The S-containing functional groups could contribute to the generation of pseudocapacitance. The above factors improve the capacitive performance of carbon materials. The co-dopants of S and O can also produce synergistic effects. Yi *et al*. used sulfate pulping black liquors containing lignin with abundant thioether bonds as a raw material to prepare O,S-co-doped lignin-derived porous carbons (EBLC-30) through pre-oxidation at 400 °C, followed by carbonization at 800 °C [94]. The O,S-co-doped lignin-derived porous carbons had an O content of 6.8 at%, a S content of 2.7 at%, and a specific surface area of up to 2923 m^2/g, showing an outstanding specific capacitance of 398 F/g at 0.5 A/g and rate performance of 200 F/g at 20 A/g, attributed to the co-dopants of O and S synergistically improving the surface wettability and conductivity of lignin-derived porous carbons, and the adsorption energy for Zn^{2+} ions. The EBLC-30//Zn ZIHCs achieved a high energy density of 141 Wh/kg at 400 W/kg and attained a high energy density of 71 Wh/kg at 16 kW/kg.

Boron (B) can replace C atom in both nitrogen and air atmospheres, altering the electronic and electrical properties of carbon structure. After doping B, the conductivity of the carbon structure can be enhanced and the pseudocapacitance can be generated, improving the capacitive performance of carbon materials. The B,N co-dopants can significantly boost the improvement of capacitive performance. Cao *et al.* [95] prepared B,N-doped lignin-derived porous carbons from alkali lignin (B/N@AC) by ammonium borate ($NH_4HB_4O_7$), combining with KOH activation at 800 °C. The B,N-doped lignin-derived porous carbons showed a nitrogen content of 0.4 at%, a boron content of 0.27 at%, and a specific surface area of 2366 m^2/g, displaying a specific capacitance of 391 F/g at 0.1 A/g and retaining 158 F/g at 20 A/g. The excellent capacitive performance is attributed to the synergistic modulation of the electronic structure and pseudocapacitance introduction by B,N co-dopants, and the presence of C-N-B bond effectively reduces adsorption barriers and improves the adsorption of cations [96]. The B/N@AC-based ZIHCs delivered an energy density of 126 Wh/kg at a power density of 75 W/kg.

3.3. Morphology design of lignin-derived porous carbon cathodes

The morphology design of lignin-derived porous carbons can enhance mass transfer efficiency and mechanical robustness to accelerate reaction kinetics and improve the utilization efficiency of active sites. Therefore, morphology design is an effective measure to optimize the capacitive performance of lignin-derived porous carbons.

Lignin with functional aromatic structure has been demonstrated for synthesizing carbon nanomaterials with different dimensions. These lignin-derived carbon nanomaterials mainly include zero-dimensional (0D) carbon spheres, hollow carbon spheres [97] and carbon flowers [63], one-dimensional (1D) carbon nanofibers [98], two-dimensional (2D) carbon nanosheets [99], and three-dimensional (3D) carbon monoliths [61]. However, limited by the synthesis difficulty, only the simply-synthesized 3D lignin-derived porous carbon monoliths and 2D lignin-derived porous carbon nanosheets have been studied for cathode materials in ZIHCs.

3D lignin-derived porous carbon monoliths have an interconnected network structure, which provides continuous pathways for rapid electron transfer [100]. In addition, 3D lignin-derived porous carbon monoliths have the largest size compared with the lignin-derived porous carbons with other dimensions, with the advantage of utilizing abundant inner space to store Zn^{2+} ions. When a few micropore-dominated structures are constructed inside lignin-derived porous carbon monoliths, the number of micropores to store $Zn(H_2O)_6^{2+}$ ions is less. Meanwhile, $Zn(H_2O)_6^{2+}$ ions need to diffuse into micropores through long pathways, resulting in poor kinetics. Limited by a smaller amount of micropores and slow kinetics, lignin-derived porous carbon monoliths exhibit poor capacitive performance, even with the high-level dopant of O and N. Ma *et al*. prepared 3D calcium lignosulfonate-derived hierarchical porous carbons by one-step carbonization at 700 °C (LHPC-700) (Fig. 14a) [59]. 3D LHPC-700 had the highest specific surface area of 599.3 m^2/g and microporosity of 70.3 %, with the O and N contents of 11.18 at% and 2.79 at%, exhibiting the highest specific capacitances of 179 F/g at 0.1 A/g and 51 F/g at 10 A/g. The LHPC-700-based ZIHCs exhibited an energy density of 63.5 Wh/kg. When few mesopore-dominated structures are constructed, the capacitance of lignin-derived porous carbon monoliths decreases while their rate performance enhances, attributed to the fewer micropores storing $Zn(H_2O)_6^{2+}$ ions and mesoporous structure accelerating kinetics. Zhu *et al*. prepared 3D LPCs by CaO template at 700 °C (LPC-700) with a specific surface area of 733.6 m^2/g, a microporosity of 36.2 % and an O content of 12.7 at% (Fig. 14b) [62]. 3D LPC-700 only delivered the specific capacitances of 170 F/g at 0.1 A/g and 65 F/g at 20 A/g. The LPC-700-based ZIHCs exhibited an energy density of 60 Wh/kg. Although it has a high O content, the capacitance is still lower, indicating that the storage of $Zn(H_2O)_6^{2+}$ ions in micropores is the key factor affecting the capacitive performance of 3D lignin-derived porous carbon monoliths. Chen *et al*. prepared 3D lignin-based porous carbons (LHPCs) from lignin-cellulose hydrogels by KOH activation at 800–1000 °C (Fig. 14c) [101]. The LHPCs prepared at 900 °C (LHPC-900) had a medium specific surface area of 1705.6 m^2/g, a microporosity of 34.5 %, and the lowest O content of 5.8 at%, exhibiting the capacitances of 236.5 F/g at 0.2 A/g and 143.8 F/g at 10 A/g. The LHPC-900-based ZIHCs delivered an energy density of 88 Wh/kg at 161 W/kg. Owing to the porous structure being greatly enriched, the capacitive performance of lignin-derived porous carbon monoliths is significantly improved even at low O levels. When the microporosity and surface heteroatom content further increase, the remarkable capac-

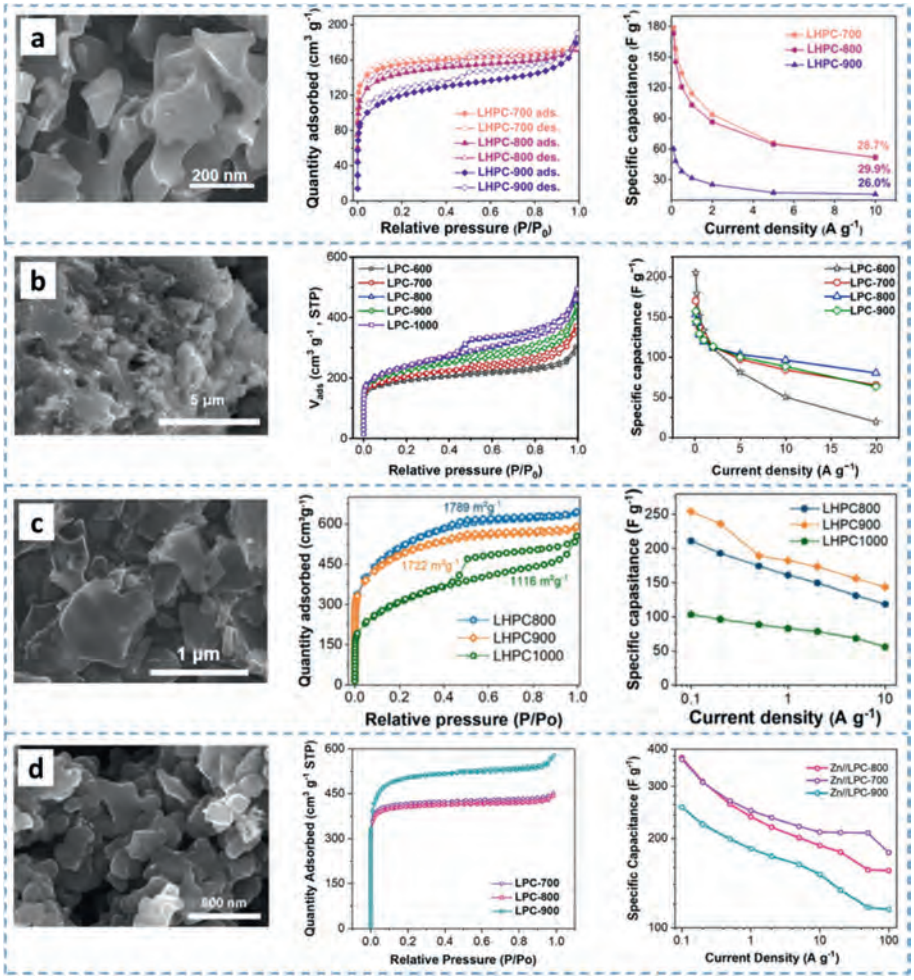


Fig. 14. Morphologies, N_2 adsorption/desorption isotherms, and capacitive performance of 3D lignin-derived porous carbon monoliths. (a) Calcium lignosulfonate-derived hierarchical porous carbon monoliths by one-step carbonization. Reproduced with permission [59]. Copyright 2023, Royal Society of Chemistry. (b) Enzymatic hydrolysis lignin-derived porous carbon monoliths by CaO template. Reproduced with permission [62]. Copyright 2023, Elsevier. (c) Lignin-based porous carbons from lignin-cellulose hydrogels by KOH activation. Reproduced with permission [101]. Copyright 2024, Elsevier. (d) Enzymatic hydrolysis lignin-derived porous carbon monoliths by $CuCl_2$ activation. Reproduced with permission [102]. Copyright 2022, Elsevier.

itive performance of lignin-derived porous carbon monoliths can be achieved. Wen *et al.* prepared 3D lignin-derived porous carbons (LPCs) by $CuCl_2$ activation at 700–900 °C (Fig. 14d) [102]. In $CuCl_2$ activation, the chloride ions in copper chloride deprived the hydrogen atoms in lignin, resulting in the loss of hydrogen atoms and the formation of pores. The LPCs prepared at 700 °C (LPC-700) had a medium specific surface area of 1628 cm^3/g, the highest microporosity of 89 %, and the highest O content of 18.1 at%, delivering a high specific capacitance of 370 F/g at 0.1 A/g and the best rate performance. The LPC-700//Zn ZIHCs displayed a high energy density of 160 Wh/kg at 101 W/kg.

Theoretically, if all inner spaces can be fully utilized to store $Zn(H_2O)_6^{2+}$ ions, with the assistance of surface heteroatom sites, the outstanding performance will be achieved for 3D lignin-derived porous carbon monoliths. Following the line of this thought, the optimal choice is to construct a microporous structure with maximum accessibility and rapid ion transport within 3D lignin-derived porous carbon monoliths, followed by a hierarchical micropore-mesopore structure. Of course, the difficulty of constructing these two porous structures also decreases in sequence.

2D nanosheets have become the primary choice for morphology design due to their high specific surface area and a large number of accessible electrochemically active sites [1,4]. However, the interactions between nanosheets make them easily restack and aggregate, resulting in a decrease in the amount of accessible electrochemically active sites and deteriorative kinetics [15,103,104], which limits the electrochemical performance.

Carbon superstructures, consisting of low-dimensional (0D, 1D, and 2D) units into 3D structures, can integrate the advantages of low-dimensional structures and 3D structures to achieve an increased exposure of surface active sites and enhanced charge transfer kinetics [15,23,104,105]. As shown in Fig. 15a, for 3D carbon monoliths, $Zn(H_2O)_6^{2+}$ ions need to enter inner storage sites through pore channels. Due to slow diffusion kinetics and high diffusion energy barriers, the deep inner sites are easily inaccessible. Besides, the number of surface storage sites is limited. Compared with 3D lignin-derived porous carbon monoliths, 2D/3D carbon superstructures can expose a larger amount of accessible surface sites for Zn^{2+} ion storage and reduce the diffusion distance for rapid Zn^{2+} ion transport. Therefore, the diffusion kinetics could be greatly improved. In addition, 2D/3D carbon superstructures can also provide multidimensional ways for the diffusion of $Zn(H_2O)_6^{2+}$ ions into inner storage sites. Zhang *et al.* used sodium lignosulfonate as a raw material to prepare 2D/3D N,O-doped lignin-derived porous carbon superstructures by supramolecular-mediated direct carbonization at 800 °C [80]. The N,O-doped lignin-derived porous carbon superstructures had a specific surface area of only 657 m^2/g, a mesoporosity of up to 90.1 %, and the con-

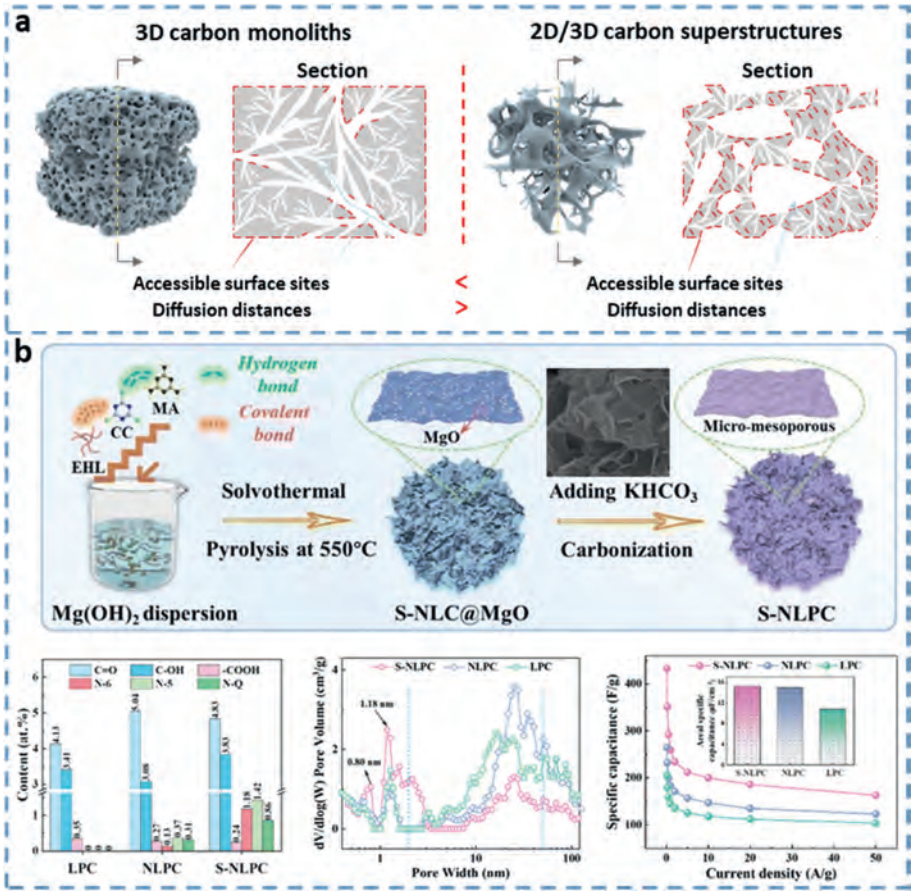


Fig. 15. (a) Schematic illustration for the difference between 3D carbon monoliths and 2D/3D carbon superstructures. (b) Preparation of 2D/3D N,O co-doped lignin-derived porous carbon superstructures by organic-inorganic supramolecular self-assembly strategy. Reproduced with permission [99]. Copyright 2025, Royal Society of Chemistry.

tents of N (14.9 at%) and O (4.7 at%), showing inferior specific capacitance (only 266 F/g at 0.05 A/g) and outstanding rate performance (113 F/g at 100 A/g). Those are attributed to limited storage sites and mesopore-accelerated reaction kinetics, respectively. Wen *et al.* used enzymatic hydrolysis lignin as a raw material to prepare 2D/3D N,O-doped lignin-derived porous carbon superstructures at 600 °C (LPCS-600) through $Cu(NO_3)_2$ activation [106]. The specific surface area and mesoporosity of LPCS-600 were 642 m^2/g and 85.4%, respectively. The N and O contents were 6.7 at% and 11.5 at%, respectively. LPCS-600 showed the specific capacitances of 301 F/g at 0.1 A/g and 127 F/g at 20 A/g. By adjusting the doping level of N and O atoms to increase surface storage sites, the capacitive performance of lignin-derived porous carbon nanosheets can be increased. The LPCS-600//Zn ZIHCs delivered an energy density of 107 Wh/kg at a power density of 86 W/kg and maintained an energy density of 45 Wh/kg at an ultra-high power density of 340,000 W/kg.

The synergistic regulation of N,O dopants and pore structure can significantly enhance the capacitive performance of 2D/3D lignin-derived porous carbon superstructures. As shown in Fig. 15b, Fan *et al.* designed an organic-inorganic supramolecular self-assembly strategy to synthesize lignin@$Mg(OH)_2$-cyanuric acid-melamine supramolecular and prepared 2D/3D N,O co-doped lignin-derived porous carbon superstructures (S-NLPC) by pre-carbonization at 550 °C and $KHCO_3$ activation at 700 °C [99]. S-NLPC had a developed porous carbon nanosheet network with a specific surface area of 2848 m^2/g, a carbonyl content of 4.8 at%, and an edge nitrogen content of 2.6 at%, showing an excellent specific capacitance of 433 F/g at 0.1 A/g and a rate performance of 191 F/g at 20 A/g. The S-NLPC//Zn ZIHCs exhibited an energy density of 122 Wh/kg at a power density of 80 W/kg and retained an energy density of 60 Wh/kg at 5300 W/kg.

The electrochemical performance of lignin-derived porous carbon cathodes for ZIHCs are summarized in Table 2. In summary, pore structure regulation and surface heteroatom modification are the dominant factors in affecting the capacitive performance of lignin-derived porous carbons, especially the pore structure regulation. The morphology design is the secondary factor in optimizing the capacitive performance of lignin-derived porous carbons.

It is well known that the composition of biomass varies greatly due to the differences in category, habitat, and growth state [54]. Lignin is an amorphous aromatic macromolecule with a highly branched three-dimensional network structure based on phenylpropane units and ether linkages [37,50,107]. The differences in the structure of lignin obtained from different biomasses, processes, and process parameters will further increase. Hou *et al.* investigated the relationship between the structures of lignin from eucalyptus, Pinus sylvestris, and bamboo and the electrochemical properties of their derived porous carbons by NaOH activation at 900 °C [108]. Compared with eucalyptus lignin and bamboo lignin, the high methoxy group content in eucalyptus lignin contributed to the formation of micropores and small-sized mesopores and facilitated the incorporation of O from the side chains of lignin into the carbon structure. The O modification reduced the adsorption energy barrier from -0.17 eV to -0.36 eV and introduced pseudocapacitance. The eucalyptus lignin-derived porous carbons (EBLC) had a specific surface area of 1599 m^2/g, a microporosity of 77.5%, and an oxygen content of 5.4 at%, displaying a higher capacitance of

Table 2
Electrochemical performance of lignin-derived porous carbon cathodes for ZIHCs.

Categories	Cathodes	Electrolyte	Potential window (V)	Current density (A/g)	Capacitance (F/g)	Cycling stability	Energy density (Wh/kg)	Power density (W/kg)	Ref.
Pore regulation	LHPC	1 mol/L $ZnSO_4$	0.1–1.8	0.1/20	261/135	99% after 5800 cycles	116	–	[84]
	LHPC-900	1 mol/L $ZnSO_4$	0.2–1.8	0.1	298	96% after 10,000 cycles	135	101	[85]
	BLC-800	1 mol/L $ZnSO_4$	0.2–1.8	0.1/20	244/150	86.6% after 10,000 cycles	85/20	359/9900	[86]
	EBLC	1 mol/L $ZnSO_4$	0.2–1.8	0.5/20	227/117	85.3% after 10,000 cycles	72/18	400/1110	[108]
	LPC-800	1 mol/L $ZnSO_4$	0.2–1.8	0.1/20	157/100	87.6% after 20,000 cycles	–	–	[71]
	NSLHPC	1 mol/L $ZnSO_4$	0.2–1.8	0.2/10	295/147	96% after 10,000 cycles	105/52	161/8500	[87]
Surface modification	ENHPC-0.5	1 mol/L $ZnSO_4$	0.2–1.8	0.1/20	350/129	99.4% after 10,000 cycles	120	80	[88]
	NLPC-800	1 mol/L $ZnSO_4$	0.2–1.8	0.1/20	357/126	94.6% after 5000 cycles	126/25	80/9677	[75]
	OLPC	1 mol/L $ZnSO_4$	0.2–1.8	0.1/20	256/105	96% after 10,000 cycles	91/37	80/16,000	[61]
	OLCK4	1 mol/L $ZnSO_4$	0.2–1.8	0.3/20	274/109	86.7% after 10,000 cycles	94/32	391/15,800	[91]
	EBLC-30	2 mol/L $ZnSO_4$	0.2–1.8	0.5/20	398/200	89.8% after 10,000 cycles	141/71	400/16,000	[94]
	B/N@AC	2 mol/L $ZnSO_4$	0.2–1.8	0.1/20	391/158	87.5% after 10,000 cycles	126/66	75/17,037	[95]
Morphology design	LHPC-700	1 mol/L $ZnSO_4$	0.2–1.8	0.1/10	179/51	82% after 8000 cycles	64	–	[59]
	LPC-700	1 mol/L $ZnSO_4$	0.2–1.8	0.1/20	170/65	92.1% after 20,000 cycles	60	–	[62]
	LHPC-900	1 mol/L $ZnSO_4$	0.2–1.8	0.2/10	237/144	99.7% after 9000 cycles	88	161	[101]
	LPC-700	1 mol/L $ZnSO_4$	0.2–1.8	0.1	370	97% after 10,000 cycles	160	101	[102]
	LNPC-800	1 mol/L $ZnSO_4$	0.2–1.8	0.05/100	266/113	99% after 10,000 cycles	–	–	[80]
	LPCS-600	1 mol/L $ZnSO_4$	0.2–1.8	0.1/20	301/127	95% after 5000 cycles	107/45	86/340,000	[106]
	S-NLPC	1 mol/L $ZnSO_4$	0.2–1.8	0.1/20	433/191	90.2% after 20,000 cycles	122/60	80/5300	[99]

227 F/g at 0.5 A/g than eucalyptus lignin-derived porous carbons (PBLC) (213 F/g, 967 m^2/g, 67.4% and 4.9 at%) and bamboo lignin-derived porous carbons (BBLC) (171 F/g, 908 m^2/g, 67.4% and 3.1 at%). EBLC also showed the best rate performance. The EBLC-based ZIHCs achieved an energy density of 71.8 Wh/kg at a power density of 400 W/kg and an energy density of 17.9 Wh/kg at 1110 W/kg.

Furthermore, Hou *et al*. explored the effect of lignin sulfidity (using Na_2S) on the electrochemical performance of its derived porous carbons by NaOH activation at 800 °C [94]. With the increase in sulfidity, the specific surface area of the prepared lignin-derived porous carbons first increased and then decreased, achieving the highest at a sulfidity of 25%. The mesoporosity decreased with increasing sulfidity. The contents of O and S increased as sulfidity increased. The lignin-derived porous carbons prepared with sulfidity exhibited higher capacitances (237.8–397.8 F/g at 0.5 A/g) and rate performance (91.4–200.3 F/g at 20 A/g) than those without sulfidity (215.8 F/g at 0.5 A/g and 79.4 F/g at 20 A/g). As sulfidity increased, the capacitances of the prepared lignin-derived porous carbons at 0.1 A/g and 20 A/g first increased and then decreased. When the sulfidity was 30%, the prepared lignin-derived porous carbons with a specific surface area of 2923 m^2/g and O/S contents of 6.8/2.7 at% delivered the highest capacitance (397.8 F/g at 0.5 A/g) and rate performance (200.3 F/g at 20 A/g). The excellent electrochemical performance can be attributed to that the high specific surface area provided abundant adsorption space and the expanded micropore size accelerated the diffusion of electrolyte ions. The O atoms primarily enhance electrochemical performance by increasing pseudocapacitance and improving the wettability of the electrode surface, and S atoms optimize electron transport pathways to promote efficient electron transfer and increase the conductivity. Moreover, the C-SO_x-C group significantly facilitates the dissolution of zinc by-products, thereby further improving the stability and cycling lifespan. The assembled ZIHCs could deliver a high energy density of 141 Wh/kg at 400 W/kg.

As the classic carbon materials, graphene oxide (GO) and reduced graphene oxide (rGO) with oxygenated groups and defects, and their composites, have also been studied as carbon cathode materials in ZIHCs. As summarized in Table 3, the pure rGO (RG-R) exhibits a low specific capacitance of 200 F/g at 0.1 A/g and poor rate capability of 128 F/g at 5 A/g, which may be ascribed to the easily-stacking characteristic of graphene [109]. Through 3D structural design, the capacitive performance of graphene hydrogel (GH) films and dense three-dimensional graphene (DGH) could be further improved [110,111]. Moreover, as graphene is chemically etched to introduce defects, the capacitance of chemically activated graphene (aMEGO) increases [112]. When defects and structural design are simultaneously performed, the capacitive performance of activated vertical graphene (A-VGN) and porous and defective graphene block (BSG) is significantly enhanced [113,114]. In addition, the oxygen-functional substituents can also improve the electrochemical performance of rGO through a hydrogen peroxide-assisted hydrothermal process (HHT-rGO) [115]. By regulating the oxygen functional groups of rGO through annealing degree, the capacitance and rate performance of rGO annealed at 200 °C (rGO-200) can be more effectively improved [116]. Furthermore, Compositing defective graphene or carbon nanotube with rGO is also

Table 3
Electrochemical performance of graphene derivatives and commercial activated carbons.

Categories	Cathodes	Electrolyte	Potential window (V)	Current density (A/g)	Capacitance (F/g)	Cycling stability	Energy density (Wh/kg)	Power density (W/kg)	Ref.
Graphene derivatives	RG-R	1 mol/L $ZnSO_4$	0–1.6	0.1/5	200/128	92 % after 10,000 cycles	–	–	[109]
	GH films	2 mol/L $ZnSO_4$	0.2–1.8	0.2/10	223/135	90 % after 10,000 cycles	53/39	3602/6539	[110]
	DGH	1 mol/L $ZnSO_4$	0.2–1.8	0.5/20	222/166	80 % after 30,000 cycles	–	–	[111]
	aMEGO	3 mol/L Zn $(CF_3SO_3)_2$	0–1.9	0.5	166	93 % after 80,000 cycles	106	–	[112]
	A-VGN	2 mol/L $ZnSO_4$	0.2–1.8	0.2/20	554/212	97.4 % after 10,000 cycles	70	70,000	[113]
	BSG	3 mol/L Zn $(CF_3SO_3)_2$	0.2–1.8	0.5/20	224/117	86 % after 10,000 cycles	–	–	[114]
	HHT-rGO	1 mol/L $ZnSO_4$	0.2–1.6	–	–	97.8 % after 20,000 cycles	75	–	[115]
	rGO-200	1 mol/L $ZnSO_4$	0.01–1.8	0.5/20	245/130	75 % after 10,000 cycles	–	–	[116]
	75 % NHG-rGO	2 mol/L $ZnSO_4$	0.3–1.6	0.1/20	198/147	93.9 % after 100,000 cycles	74	75	[117]
	P-CNT/rGO	2 mol/L $ZnSO_4$	0.2–1.8	0.5/100	213/119	94.2 % after 10,000 cycles	93/42	80/80,000	[118]
Commercial activated carbons	YP-50F	1 mol/L $ZnSO_4$	0.2–1.8	0.1/20	165/67	–	59	80	[75]
	AC	2 mol/L $ZnSO_4$	0.2–1.8	0.1/20	272/92	91 % after 10,000 cycles	84/30	69/14,900	[119]

a pathway to enhance its electrochemical performance, such as N_2H_4-graphene/rGO (75 %NHG-rGO) and phosphorus-doped carbon nanotube/reduced graphene oxide aerogel (P-CNT/rGO) [117,118]. Compared with the graphene derivatives as cathode materials for ZIHCs, the lignin-derived porous carbons show higher capacitances, and the assembled ZIHCs show higher energy densities. The rate capabilities between graphene derivatives and lignin-derived porous carbons are similar, while the cycling life of lignin-derived porous carbons is relatively short. Lignin-derived porous carbons also have a cost superiority to graphene derivatives.

Commercial activated carbons, with high specific surface area and good spatial structure, have naturally been studied as cathode materials for ZIHCs. As shown in Table 3, the YP-50 activated carbon from Kuraray Chemical Co., Ltd. in Japan only displays low capacitances of 165/67 F/g at 0.1/20 A/g, and the assembled ZIHCs exhibit an energy density of 59 Wh/kg at 80 W/kg [75]. The activated carbon (AC) from Nanjing XFNANO Materials Tech Co., Ltd. in China shows enhanced electrochemical performance, as well as the assembled ZIHCs [119]. The capacitance and rate capability of these commercial activated carbons are far inferior to that of lignin-derived porous carbons, especially rate capability. However, the structural consistency of lignin-derived porous carbons is quite bad compared to commercial activated carbons. This is a big obstacle in the practical development of lignin-derived porous carbon cathodes for ZIHCs.

4. Summary and perspectives

Based on the unique characteristics of high carbon content, high aromaticity, and functional molecular structure, high-performance porous carbons can be developed from renewable lignin for its high-value application in ZIHCs. The main conclusions are summarized as follows.

(1) The pore structure is the main factor affecting the capacitive performance of lignin-derived porous carbons, followed by surface heteroatom dopants, and finally morphology dimension design. The micropores with the sizes larger than 0.68 nm could effectively store $Zn(H_2O)_6^{2+}$ ions, and the large micropores with the sizes of 1–2 nm can serve as transport channels. Mesopores could accelerate the transportation of $Zn(H_2O)_6^{2+}$ ions. Hierarchical micropore-small mesopore structure and hierarchical micropore-wide mesopore structure can both enable high capacitive performance for lignin-derived porous carbons.
(2) The specific heteroatom configurations can significantly improve the capacitive performance of lignin-derived porous carbon cathodes, and the dual active heteroatom configurations could produce a synergistic effect to further enhance capacitive performance. The dopants of N and O exhibit outstanding advantages in this respect.
(3) The morphological dimension design is an effective approach to improve electrochemical kinetics and the utilization efficiency of active sites, optimizing the capacitive performance of lignin-derived porous carbons. It is difficult to construct a suitable porous structure inside 3D lignin-derived porous carbon monoliths to fully utilize the inner space. The kinetics of $Zn(H_2O)_6^{2+}$ ions into inner storage sites through pore channels is slow, limiting the capacitive performance of 3D lignin-derived porous carbons. By contrast, 2D/3D lignin-derived porous carbon superstructures can easily provide a larger amount of accessible surface sites and faster kinetics *via* multidimensional diffusion ways.

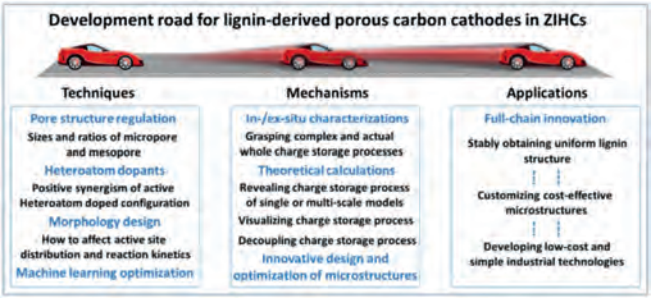


Fig. 16. The proposed development directions of lignin-derived porous carbons.

From a long-term and sustainable perspective, we propose the development direction of lignin-derived porous carbon cathodes to address potential technical, mechanistic, and application-level challenges in the future (Fig. 16).

(1) The ingenious strategies could be developed to precisely and solely adjust pore structure, heteroatom-doped configuration, or morphology without causing other structural changes for comprehensively understanding the structure-capacitive performance relationship, which is the foundation for the preparation of high-performance lignin-derived porous carbons. Specifically, micropores and mesopores are crucial for storing and transporting hydrated Zn^{2+} ions. Determining the appropriate sizes and ratios of micropore and mesopore is particularly important for efficient Zn^{2+} ion storage. The active configura-

tion caused by a single heteroatom dopant is clear. However, the synergistic enhancement of efficient Zn^{2+} ion storage by different active heteroatom-doped configurations is still challenging. The influence of morphology dimensions (especially 0D and 1D) on the capacitive performance of lignin-derived porous carbons is missing. The effect of morphology on the active site distribution and electrochemical reaction kinetics also needs to be clarified. By using machine learning techniques, the multi-dimensional coupling relationships among preparation technique, pore structure, heteroatom doping, morphology structure, and capacitive performance are further established to assist the optimal preparation of high-performance lignin-derived porous carbons with ideal microstructures.

(2) The advanced electrochemical characterizations, such as *in-situ* or *ex-situ* XRD, SEM, XPS, and EQCM, are used to comprehensively grasp the complex dynamic charge storage processes. Based on the theoretical calculations, the interactions between single or multi-scale models and Zn ions are revealed and visualized in depth at the atomic-molecular level. By combining advanced characterizations and theoretical calculations, the complex charge storage process is decoupled to exploit charge storage mechanisms, providing theoretical guidance for the innovative design and optimization of microstructures.

(3) The stable acquisition of uniform lignin structure is a prerequisite for industrial production of lignin-derived porous carbons. However, the influence of lignin chemical structure on the microstructures and electrochemical properties of lignin-derived porous carbons should be clarified as much as possible. Based on the original laboratory processes and the specific structural characteristics of lignin, the process cost, structure, and performance should be balanced to customize cost-effective microstructures. Simultaneously, the low-cost, simple, and greener industrial technologies (such as deep eutectic solvent treatment, self-activation, and Joule thermal carbonization) to prepare lignin-derived porous carbons with ideal microstructures are being developed to achieve the full-chain innovation, which is promising to solve the application problems of lignin-derived porous carbon cathodes.

Declaration of competing interest

The authors declare that they have no known competing financial interests or personal relationships that could have appeared to influence the work reported in this paper.

CRediT authorship contribution statement

Caiwei Wang: Writing – original draft, Visualization, Funding acquisition, Data curation, Conceptualization. **Cheng Zeng:** Writing – review & editing, Investigation. **Changhong Wei:** Writing – review & editing, Investigation. **Guizhen Chen:** Writing – review & editing. **Yueling Liang:** Writing – review & editing. **Wenli Zhang:** Writing – review & editing, Funding acquisition, Conceptualization.

Acknowledgments

This work was supported by the National Natural Science Foundation of China (No. 22408061), Natural Science Foundation of Guangxi Province (No. 2025GXNSFBA069417), the Dean Project of Guangxi Key Laboratory of Petrochemical Resource Processing and Process Intensification Technology (No. 2023Z014), and the Open Foundation of Shanghai Jiao Tong University Shaoxing Research Institute of Renewable Energy and Molecular Engineering (No. JDSX2023002). Caiwei Wang acknowledges the financial support from the Program for Introducing High-Level Talents from Guangxi University.

Supplementary materials

Supplementary material associated with this article can be found, in the online version, at doi:10.1016/j.cclet.2025.111850.

References

[1] Y. Wang, S. Sun, X. Wu, et al., Nano-Micro Lett. 15 (2023) 78.
[2] J. Yin, W. Zhang, N.A. Alhebshi, et al., Adv. Energy Mater. 11 (2021) 2100201.
[3] J. Zhu, J. Tai, T. Liu, et al., Adv. Energy Mater. 15 (2024) 2403739.
[4] M. Peng, C. Xue, M. Yang, et al., Energy Storage Mater. 74 (2025) 103945.
[5] T. Shi, Z. Song, Y. Lv, et al., Chin. Chem. Lett. 36 (2025) 109559.
[6] Y. Chen, Z. Song, Y. Lv, et al., Nano-Micro Lett. 17 (2025) 117.
[7] C. Zhu, H. Liang, P. Li, et al., J. Energy Chem. 100 (2025) 637–645.
[8] C. Zhu, R. Long, L. Zhu, et al., J. Colloid Interface Sci. 652 (2023) 590–598.
[9] Y. Zhang, C. Zhu, Y. Xiong, et al., Small Methods 7 (2023) 2300714.
[10] C. Zhu, H. Wang, W. Fan, et al., Rare Met. 41 (2022) 2505–2516.
[11] Y. Liu, L. Wu, Nano Energy 109 (2023) 108290.
[12] Y. Shao, M.F. El-Kady, J. Sun, et al., Chem. Rev. 118 (2018) 9233–9280.
[13] G. Yang, Z. Hao, C. Fang, et al., Chin. Chem. Lett. 36 (2025) 111185.
[14] S. Xin, X. Zhang, L. Wang, et al., Sci. China Chem. 67 (2024) 13–42.
[15] C. Hu, P. Liu, Z. Song, et al., Chin. Chem. Lett. 36 (2025) 110381.
[16] L. Yu, J. Li, N. Ahmad, et al., J. Mater. Chem. A 12 (2024) 9400–9420.
[17] H. Zhang, J. Zhang, Y. Liu, et al., Coord. Chem. Rev. 482 (2023) 215056.
[18] F. Wei, Y. Zeng, Y. Guo, et al., Chem. Eng. J. 468 (2023) 143576.
[19] L. Miao, Y. Lv, D. Zhu, et al., Chin. Chem. Lett. 34 (2023) 107784.
[20] G. Yang, Q. Zhang, C. He, et al., Angew. Chem. Int. Ed. 64 (2025) e202421230.
[21] J. Li, K. Ge, A.O. Grammenos, et al., Adv. Mater. 37 (2025) 2502422.
[22] X. Li, C. Cai, P. Hu, et al., Adv. Mater. 36 (2024) 2400184.
[23] Y. Long, X. An, Y. Yang, et al., Adv. Funct. Mater. 35 (2025) 2424551.
[24] K. Xiao, X. Jiang, S. Zeng, et al., Adv. Funct. Mater. 34 (2024) 2405830.
[25] Q. Song, L. Jiang, H. Chen, et al., Energy Storage Mater. 77 (2025) 104219.
[26] R. Madhu, A.P. Periasamy, P. Schlee, et al., Carbon 207 (2023) 172–197.
[27] W. Li, G. Wang, W. Sui, et al., Int. J. Biol. Macromol. 234 (2023) 123603.
[28] P. Feng, H. Wang, P. Huang, et al., Chem. Eng. J. 471 (2023) 144817.
[29] Y. Du, G. Sun, Y. Li, et al., Carbon 178 (2021) 243–255.
[30] X. Lin, Y. Liu, H. Tan, et al., Carbon 157 (2020) 316–323.
[31] C. Wang, D. Yang, W. Zhang, et al., ACS Appl. Mater. Interfaces 15 (2023) 4371–4384.
[32] L. Huang, Z. Gu, J. Gu, et al., Green Chem. 26 (2024) 10196–10204.
[33] S. Huang, D. Yang, X. Qiu, et al., Adv. Funct. Mater. 32 (2022) 2203279.
[34] J. Zhu, C. Yan, X. Zhang, et al., Prog. Energy Combust. Sci. 76 (2020) 100788.
[35] B. Jiang, H. Jiao, X. Guo, et al., Adv. Sci. 10 (2023) 2206055.
[36] Z. Liu, Y. Yu, Y. Liu, et al., ACS Catal. 14 (2024) 2115–2126.
[37] W. Zhang, X. Qiu, C. Wang, et al., Carbon Res. 1 (2022) 14.
[38] C. Liu, J. Hu, H. Zhang, et al., Fuel 182 (2016) 864–870.
[39] C. Wang, S. Zhang, S. Wu, et al., Bioresour. Technol. 254 (2018) 231–238.
[40] C. Wang, S. Zhang, S. Wu, et al., Bioresour. Technol. 263 (2018) 289–296.
[41] C. Wang, S. Huang, Y. Zhu, et al., J. Anal. Appl. Pyrolysis 161 (2022) 105408.
[42] Y. Wang, C. Ding, J. Chen, et al., Environ. Sci. Wat. Res. Technol. 9 (2023) 948–956.
[43] R.A. Fenner, J.O. Lephardt, J. Agric. Food Chem. 29 (1981) 846–849.
[44] Q. Liu, S. Wang, Y. Zheng, et al., J. Anal. Appl. Pyrolysis 82 (2008) 170–177.
[45] J. Hu, R. Xiao, D. Shen, et al., Bioresour. Technol. 128 (2013) 633–639.
[46] B. Li, W. Lv, Q. Zhang, et al., J. Anal. Appl. Pyrolysis 108 (2014) 295–300.
[47] Z. Jing, X. Wang, H. Jun, et al., Polym. Degrad. Stab. 108 (2014) 133–138.
[48] Z. Guo, Y. Yin, M. Nie, et al., J. Agric. Food Chem. 73 (2025) 3142–3153.
[49] Y. Wang, Z. Yi, L. Xie, et al., Adv. Mater. 36 (2024) 2401249.
[50] C. Wang, D. Yang, X. Qiu, et al., Prog. Chem. 34 (2022) 285.
[51] J. Zakzeski, P.C. Bruijnincx, A.L. Jongerius, et al., Chem. Rev. 110 (2010) 3552–3599.
[52] F. Torres-Canas, A. Bentaleb, M. Föllmer, et al., Carbon 163 (2020) 120–127.
[53] S. Yang, Z. Zhang, X. Qiu, et al., Resour. Chem. Mater. 2 (2023) 245–251.
[54] C. Wang, W. Zhang, X. Qiu, et al., EnergyChem 6 (2024) 100133.
[55] Q. Meng, B. Chen, W. Jian, et al., J. Power Sources 581 (2023) 233475.
[56] Q. Wu, W. Shao, Y. Zhang, et al., BioResources 15 (2020) 105–116.
[57] W. Jian, W. Zhang, X. Wei, et al., Adv. Funct. Mater. 32 (2022) 2209914.
[58] Y. Lin, Y. Hwang, K. Chan, et al., Ind. Crops Prod. 221 (2024) 119330.
[59] J. Ma, S. Yang, T. Huang, et al., New J. Chem. 47 (2023) 17549–17557.
[60] S. Beak, S. Kim, S. Oh, et al., J. Environ. Chem. Eng. 13 (2025) 116086.
[61] X. Liang, C. Wang, Z. Li, et al., Resour. Chem. Mater. 4 (2025) 100089.
[62] J. Zhu, X. Qiu, S. Sun, et al., J. Cleaner Prod. 419 (2023) 138201.
[63] B. Zhang, D. Yang, X. Qiu, et al., Carbon 162 (2020) 256–266.
[64] Y. Song, J. Liu, K. Sun, et al., RSC Adv. 7 (2017) 48324–48332.
[65] S. Huang, D. Yang, W. Zhang, et al., Microporous Mesoporous Mater. 317 (2021) 111004.
[66] X. Zhang, H. Lu, K. Wu, et al., Fuel 363 (2024) 130835.
[67] K. Wu, C. Yang, Y. Liu, et al., Catal. Today 365 (2021) 214–222.
[68] F. Fu, D. Yang, Y. Fan, et al., J. Colloid Interface Sci. 628 (2022) 90–99.
[69] F. Fu, D. Yang, B. Zhao, et al., J. Colloid Interface Sci. 640 (2023) 698–709.
[70] Y. Xi, S. Huang, D. Yang, et al., Green Chem. 22 (2020) 4321–4330.
[71] J. Zhu, T. Huang, M. Lu, et al., Green Chem. 26 (2024) 5441–5451.
[72] Y. Xi, X. Ji, F. Kong, et al., Polymers 16 (2024) 201.
[73] F. Fu, D. Yang, W. Zhang, et al., Chem. Eng. J. 392 (2020) 123721.
[74] C. Wang, D. Yang, S. Huang, et al., Green Chem. 24 (2022) 5941–5951.

[75] Z. Li, C. Wang, Y. He, et al., J. Power Sources 635 (2025) 236543.
[76] L. Wang, M. Peng, J. Chen, et al., Adv. Mater. 34 (2022) 2203744.
[77] T. Huang, Y. Wu, G. Liu, et al., J. Power Sources 646 (2025) 237282.
[78] L. Xie, F. Su, L. Xie, et al., Mat. Chem. Front. 4 (2020) 2610–2634.
[79] X. Zhang, C. Yu, Y. Xie, et al., J. Mater. Chem. A 12 (2024) 12054–12063.
[80] W. Zhang, J. Yin, W. Jian, et al., Nano Energy 103 (2022) 107827.
[81] J. Guo, T. Wang, D. Wu, et al., Chem. Eng. J. 506 (2025) 160245.
[82] H. Li, P. Su, Q. Liao, et al., Small 19 (2023) 2304172.
[83] Z. Dang, X. Li, Y. Li, et al., J. Colloid Interface Sci. 644 (2023) 221–229.
[84] W. Zhang, W. Jian, J. Yin, et al., J. Cleaner Prod. 327 (2021) 129522.
[85] L. Zhao, W. Jian, X. Zhang, et al., J. Energy Storage 53 (2022) 105095.
[86] Y. Yi, S. Hu, C. Liu, et al., J. Colloid Interface Sci. 675 (2024) 569–579.
[87] Y. Fan, F. Fu, D. Yang, et al., J. Colloid Interface Sci. 667 (2024) 147–156.
[88] C. Wang, Z. Li, W. Zhang, et al., J. Colloid Interface Sci. 685 (2025) 674–684.
[89] L. Zhao, W. Jian, J. Zhu, et al., ACS Appl. Mater. Interfaces 14 (2022) 43431–43441.
[90] Z. Yang, X. Chang, H. Mi, et al., J. Colloid Interface Sci. 658 (2024) 506–517.
[91] H. Zhang, L. Wang, Y. Zhang, et al., J. Colloid Interface Sci. 635 (2023) 94–104.
[92] H. He, J. Lian, C. Chen, et al., Nano-Micro Lett. 14 (2022) 106.
[93] B. Xue, C. Liu, X. Wang, et al., Chem. Eng. J. 480 (2024) 147994.
[94] Y. Yi, S. Hu, Y. Ma, et al., Chem. Eng. J. 509 (2025) 161224.
[95] T. Cao, W. Li, J. Zhu, et al., Energy Convers. Manage. 326 (2025) 119498.
[96] W. Feng, N. Feng, W. Liu, et al., Adv. Energy Mater. 11 (2020) 2003215.
[97] Y. Liang, Y. Yu, X. Qi, Int. J. Biol. Macromol. 307 (2025) 141938.
[98] J. Li, D. Guo, Q. Wang, et al., Int. J. Biol. Macromol. 307 (2025) 141921.
[99] Y. Fan, D. Yang, F. Fu, et al., Green Chem. 27 (2025) 3932–3943.
[100] C. Wang, D. Yang, Y. Zhu, et al., Ind. Crops Prod. 180 (2022) 114748.
[101] F. Chen, Y. Zheng, W. Jian, et al., J. Energy Storage 108 (2025) 115163.
[102] F. Wen, W. Zhang, W. Jian, et al., Chem. Eng. Sci. 255 (2022) 117672.
[103] L. Gao, X. Zhong, Z. Li, et al., Chem. Commun. 60 (2024) 1269–1272.
[104] S. Jha, Y. Qin, Y. Chen, et al., J. Mater. Chem. A 13 (2025) 15101–15110.
[105] P. Liu, Z. Song, L. Miao, et al., Small 20 (2024) 2400774.
[106] F. Wen, Y. Yan, S. Sun, et al., J. Colloid Interface Sci. 640 (2023) 1029–1039.
[107] W. Zhang, J. Yin, C. Wang, et al., Small Methods 5 (2021) 2100896.
[108] Y. Yi, S. Hu, Y. Ma, et al., J. Colloid Interface Sci. 683 (2025) 55–67.
[109] G. Sun, Y. Xiao, B. Lu, et al., ACS Appl. Mater. Interfaces 12 (2020) 7239–7248.
[110] Y. Zhu, X. Ye, H. Jiang, et al., J. Power Sources 453 (2020) 227851.
[111] L. Zhang, D. Wu, G. Wang, et al., Chin. Chem. Lett. 32 (2021) 926–931.
[112] S. Wu, Y. Chen, T. Jiao, et al., Adv. Energy Mater. 9 (2019) 1902915.
[113] X. Li, Y. Li, X. Zhao, et al., Energy Storage Mater. 53 (2022) 505–513.
[114] R. Yuan, H. Wang, L. Shang, et al., ACS Appl. Mater. Interfaces 15 (2023) 3006–3016.
[115] Y. Shao, Z. Sun, Z. Tian, et al., Adv. Funct. Mater. 31 (2021) 2007843.
[116] H. Xu, W. He, Z. Li, et al., Adv. Funct. Mater. 32 (2022) 2111131.
[117] J. Luo, L. Xu, H. Liu, et al., Adv. Funct. Mater. 32 (2022) 2112151.
[118] J. Yao, F. Li, R. Zhou, et al., Chin. Chem. Lett. 35 (2024) 108354.
[119] L. Dong, X. Ma, Y. Li, et al., Energy Storage Mater. 13 (2018) 96–102.